Transcription activation is enhanced by multivalent interactions independent of liquid-liquid phase separation

Jorge Trojanowski[1,§], Lukas Frank[1,§], Anne Rademacher[1],
Pranas Grigaitis[1,2] and Karsten Rippe[1,*]

[1] Division of Chromatin Networks, German Cancer Research Center (DKFZ) and Bioquant, Heidelberg, Germany

[2] present address: Systems Biology Lab, Amsterdam Institute of Molecular and Life Sciences (AIMMS), Amsterdam, The Netherlands

[§] These authors contributed equally to this work

* Address correspondence to Karsten Rippe (karsten.rippe@dkfz.de)

Keywords: gene regulation; phase-separation; transcription factor; transcription dynamics; residence time; CRISPR; dCas9; optogenetics; BRD4; acetylation; kinetic proofreading; multivalent interactions

1

Abstract

Transcription factors (TFs) consist of a DNA binding and an activation domain (AD) that are considered to be independent and exchangeable modules. However, recent studies conclude that also the physico-chemical properties of the AD can control TF assembly at chromatin via driving a phase separation into "transcriptional condensates". Here, we dissected the mechanism of transcription activation at a reporter gene array with real-time single-cell fluorescence microscopy readouts. Our comparison of different synthetic TFs reveals that the phase separation propensity of the AD correlates with high transcription activation capacity by increasing binding site occupancy, residence time and the recruitment of co-activators. However, we find that the actual formation of phase separated TF liquid-like droplets has a neutral or inhibitory effect on transcription induction. Thus, our study suggests that the ability of a TF to phase separate reflects the functionally important property of the AD to establish multivalent interactions but does not by itself enhance transcription.

Introduction

The induction of gene expression in eukaryotes involves the binding of transcription factors (TFs) and co-activators at the promoter to induce the assembly of the active RNA polymerase transcription machinery (*1-3*). The vast majority of TFs contain a structurally well-defined DNA-binding domain (DBD) and a separate activation domain (AD) (*4*). This AD typically comprises intrinsically disordered regions (IDRs) with acidic residues that keep aromatic residues exposed to the solvent (*5*). Synthetic TFs have been successfully constructed by combining DBDs and ADs in a modular manner (*6-8*). Frequently employed ADs are VP16 from a herpes simplex virus protein (*6*) and VPR (VP64-p65-Rta), a tripartite synthetic construct that consists of VP64 (4 copies of VP16) fused to the p65 and Rta ADs (*8*). The promoter binding site occupancy θ of the DBD has long been recognized as a key factor that regulates the strength of transcriptional activation (*9*). The value of θ is determined by the free TF concentration [TF] and the ratio of the kinetic on- and off-rates for binding: $\theta = [TF]/([TF] + k_{off}/k_{on})$. Thus, the target sites become fully saturated if TF concentrations are sufficiently high. In addition, a number of studies report that not only binding site occupancy but also TF residence time as given by $\tau_{res} = 1/k_{off}$ determines the transcriptional activation capacity (*10-15*). The value of τ_{res} becomes rate limiting for a multi-step activation process in which a TF binding event with a certain duration is required to drive a subsequent reaction that induces transcription. The TF chromatin interactions have long been considered to be mostly determined by the DBD. However, a number of recent studies showed that TF assembly at chromatin is not limited to direct interactions of the DBD with DNA. The IDRs found in TFs like SP1, TAF15, OCT4, β-catenin, STAT3 and SMAD3 as well as transcriptional co-activators like MED1/19,

2

GCN4 and BRD4 and the unstructured C-terminal domain (CTD) of RNA polymerase II can drive the formation of so-called "transcriptional condensates" that refer to the accumulation of these proteins at enhancers and promoters (16-20). One mechanism frequently invoked for this process is that of a liquid-liquid phase separation (LLPS). In this type of chromatin compartment proteins and RNAs form droplets that sequester their constituting components from the surrounding cytoplasm, like oil drops in water. LLPS arises via transient multivalent interactions of intrinsically disordered protein domains, creating an exclusionary local protein-RNA environment (21-24). The formation of liquid-like protein droplets could have a number of important functional implications to (i) enhance TF binding site occupancy and residence time, (ii) mediate the recruitment of co-activators, (ii) reduce target site search time (25), (iv) contribute to TF target site selection (26) and (v) enhance transcription (27, 28). However, alternative mechanisms to phase separation exist for the assembly of transcriptionally active or silenced subcompartments that include classical (cooperative) chromatin binding and formation of well-defined multi-subunit protein complexes (18, 29-32). Furthermore, showing that the formation of TF droplets indeed amplifies gene expression would require the comparison of the TF droplet state to the same TF construct bound to chromatin but without droplet formation. Such a comparison is missing in current studies.

Here, we have studied a panel of constitutive and light-inducible synthetic TF constructs with dead-Cas9 (dCas9), *tet* repressor (rTetR) and *lac* repressor (LacI) as DBDs and different ADs. The different TF architectures were evaluated with respect to their capacity of activating a reporter gene array with real-time single-cell fluorescence microscopy readouts, their activator residence times and assessing the contribution of liquid droplet formation. We find striking differences in chromatin bound residence time, RNA production, histone H3 acetylation at lysine 27 (H3K27ac) and BRD4 recruitment between different TF constructs. Furthermore, we link the phase separation propensity of the AD to TF DNA binding properties and activation capacity. Based on our results we conclude that the ability of a TF to engage in multivalent interactions enhances its activation strength and increases its propensity to form liquid droplets. However, we find no evidence that the formation of liquid droplets per se would enhance transcription.

Results

The interplay of DBDs and ADs can be probed with synthetic constructs

We studied a range of TF architectures by creating a toolbox of single- and multi-component transcriptional activation complexes (**Fig. 1A, left**). The three DBDs employed were reverse *tet* repressor (rTetR, DNA binding in the presence of doxycycline), *lac* repressor (LacI) and dead-Cas9 (dCas9) with different single guide RNAs (sgRNA) binding to *lacO* and *tet*O

operator sites. ADs were linked with the DBD module via 4 different approaches: protein fusion constructs ("fusion"), binding to PP7 RNA loops engineered into the sgRNA ("loop"), light-induced heterodimer formation between PHR-AD and DBD-CIBN fusion proteins (blue light induced chromatin recruitment, "BLInCR" (*33, 34*)) as well as light-induced binding to sgRNA loops with PP7-sgRNA, tdPCP-CIBN and PHR-AD constructs ("BLInCR-loop"). The CIBN-dCas9-CIBN localizer of the BLInCR-dCas9 system corresponds to the construct used in the LACE system by Polstein et al. (*35*). Our toolbox comprised 14 dCas9-based and 12 bacterial repressor-based possible TF construct combinations to study DNA binding, self-interaction and activation properties with fluorescence microscopy readouts (**Fig. 1A, Fig. S1, Table S1, S2**) in the human U2OS 2-6-3 reporter cell line (*36*). The latter has a reporter gene array integrated that enables time-resolved measurements to follow TF binding to *lac*O and/or *tet*O repeats and co-factor recruitment upstream of a CMV core promoter in single living cells. RNA production was visualized by binding of fluorescently tagged MS2 coat protein (tdMCP) to the 24 copies of the MS2 binding sequences engineered into the transcript of the reporter gene. The binding and dissociation of the BLInCR TFs with either dCas9 or LacI/rTetR (*34*) as DBD could be controlled by illumination with blue light (**Fig. S1A, B**). The alternating structure of *lacO* and *tetO* site clusters of the reporter array became visible upon activation by VPR recruited to *tetO* via dCas9, labeling of the *lacO* sites with fluorescent LacI and applying super-resolution radial fluctuations (SRRF) microscopy (*37*) (**Fig. 1B, top; Fig. S1C**). Chromatin decondensation induced by dCas9-GFP-VPR allowed it to distinguish separate clusters of reporter units. PHR-GFP-VPR recruited via BLInCR-dCas9 induced additional nuclear punctae outside the reporter array corresponding to optodroplets (*38*) (**Fig. 1B bottom**). The granular GFP signal at the dCas9-bound reporter array indicated that the reporter cluster was not immersed in a single homogenous droplet under these conditions. In this cellular system all four different types of TF constructs carrying the fluorescently tagged VP16 AD became robustly enriched at the reporter array when using dCas9 with a sgRNA targeting the *lacO* sites as DBD (**Fig. 1C, 1D**). To evaluate the phase separation propensity of the AD in living cells and under conditions compatible with reporter array activation, we applied a variation of the previously reported optodroplet approach (*32, 38*) (**Fig. 1E**). The activation domains of VP16, p65, Rta, STAT2 and VPR were fused to the PHR domain and recruited to the reporter *tetO* sites using the BLInCR rTetR construct. After blue light illumination, all PHR-AD fusions accumulated at the reporter array. Additional PHR-GFP-AD optodroplets formed to a very different extent. Thus, the propensity of the AD used in our toolbox to form droplets covered a broad range.

Activation strength correlates with phase separation propensity

A quantification of optodroplet formation with the constructs depicted in **Fig. 1E** was conducted

4

by determining the fraction of cells with visible optodroplets. It ranged between < 1 % (STAT2), 27 % (VP16), 41 % (Rta), 71 % (p65) and 89 % (VPR) (**Table S3**)**.** For each PHR-GFP-AD construct we also measured the coefficient of variation (CV) of its nuclear signal as a measure of droplet abundance in dependence of concentration (**Fig. S2A**). The nuclear intensity at which the CV crossed an empirically defined threshold was then used as a critical concentration for droplet formation and ranged from 0.22 a. u. for VPR with a high self-interaction propensity to 0.45 (VP16) and 0.70 a. u. (STAT2) that displayed a low capacity to form optodroplets (**Table S3**). For the BLInCR and BLInCR-loop dCas9 complexes the optodroplet propensity was slightly reduced in comparison to CIBN-rTetR but showed the same trend between VP16 and VPR. The ectopic PHR-GFP-AD assemblies displayed liquid droplet-like properties like fusion, higher mobility compared to the reporter array spot and predominantly fast exchange with the nucleoplasm as determined by fluorescence recovery after photobleaching (FRAP) (**Fig. S2B, C**). Next, we compared the potential of a given AD to induce transcription of the reporter array by monitoring nascent RNA production via tdMCP-tdTomato (**Fig. 2A**). The ADs were recruited to the reporter by light-induced binding of PHR-GFP-AD to CIBN-rTetR and single cell RNA production trajectories were recorded (**Fig. 2A, image series**). All ADs were able to elicit a transcriptional response and the activator strength positively correlated with their propensity to form optodroplets (**Fig. 2B-D**, **Table S3, S4**): (i) The time courses displayed higher maximum transcription levels of 1.7-2.9 a. u. for p65, Rta and VPR as compared to 1.3-1.6 a. u. for VP16 and STAT2 ($p<0.001$, two-way ANOVA) (**Fig. 2B, S2D**). (ii) The fraction of responding cells was larger with 67-92 % (p65, Rta, VPR) vs. 42-67 % (VP16, STAT2) (**Fig. 2C**). (iii) The time to reach half-maximal activation was shorter with 26-28 min (p65, Rta, VPR) compared to 38-42 min (VP16, STAT2) (**Table S4, Fig. S2E**) and was anticorrelated with the critical concentration for droplet formation (**Fig. 2D**). Thus, the strong transcriptional activators p65, Rta and VPR showed a high phase separation propensity while VP16 and STAT2 were weaker activators with a low tendency to form liquid droplets.

Phase-separated TF compartments are not required for efficient transcription

Next, we tested for a given AD whether activation was higher in those cells that formed phase separated AD optodroplets. The RNA time course data were split into two groups with and without visible optodroplets. In this comparison we found no enhanced activation but rather a weak repression for time courses that displayed optodroplet formation (**Fig. 2E**). There was no significant difference in the maximum value of RNA production for cells with and without droplet formation ($p > 0.05$ in pairwise t-test and in two-way ANOVA) (**Fig. 2F, Table S4**). While the time to half activation was clearly influenced by the type of AD, activation speed was unchanged or even moderately decreased if droplets were present (droplets: $0.05 \leq p \leq 0.10$, two-way ANOVA accounting for ADs and droplets) (**Fig. 2G**). The time to half-maximal

5

activation was increased from 25 ± 6 min without droplets to 30 ± 9 min for VPR (Rta: 25 ± 4 to 31 ± 5 min, p65: unchanged at 26 ± 8 min). We conclude that for a given AD, droplet formation does not enhance transcription activation but rather displayed a trend to a moderate inhibition.

Next, we tested if enhancing droplet formation of PHR-GFP-VP16, a construct with low self-interaction propensity, affects transcription dynamics and output by applying three independent perturbation approaches (**Fig. 3A**): (i) Co-transfection with CIBN-LacI, which can act as a bridging factor between PHR-AD molecules via LacI-LacI dimers or tetramers (*39*). (ii) Increasing the droplet formation propensity by binding of a second PHR domain to the AD via a GFP binding protein (GBP) construct, which will generate bivalent VP16 complexes. (iii) Fusion of PHR-GFP-VP16 to the N-terminal IDR of the FUS (fused in sarcoma) protein with reportedly high propensity to form liquid droplets *in vitro* and *in vivo* (*40*). PHR-GFP-VP16 was recruited to the reporter *tetO* sites by light via the BLInCR rTetR complex. CIBN-LacI co-transfection led to increased PHR-GFP-VP16 droplet formation shortly after illumination and lowered the critical droplet forming concentration (**Fig. 3B, top row, Fig. S3A, Table S3**). Moreover, it induced recruitment of additional PHR-GFP-VP16 molecules and increased the VP16 concentration around the promoter (**Fig. S3B**). Measurements of nascent RNA production dynamics in the presence of CIBN-LacI in addition to CIBN-rTetR (**Fig. 3C, Fig. S3C**) revealed a reduction in promoter activity, a decrease in the fraction of responding cells from 70 to 24 % and a more than 2-fold reduction of bulk RNA levels (**Fig. 3C-E, Fig S3C-D**). Co-transfection of the GFP-LacI control with CIBN-rTetR revealed some repression but this effect was smaller than the repression by formation of CIBN-LacI driven optodroplets. The activation capacity was similar to omitting the CIBN-rTetR construct, i. e. only binding of the activator to distal *lacO* sites. Co-transfection of PHR-GBP or fusion to FUSN were equally effective in inducing droplet formation of PHR-GFP-VP16 (**Fig 3F, Fig. S3E**). However, nascent RNA time courses showed near complete repression by PHR-GBP with respect to the maximum value and responder fraction while activation was largely increased for the FUSN-VP16 construct without effects on the kinetics (**Fig 3G-H, Fig S3F**). Bulk RNA levels consistently showed a similar response and displayed a 10-fold increase for FUSN-VP16 (**Fig 3I**), similar to another FUSN-VP16 construct studied recently (*28*). Thus, increasing the multivalent interaction capacity of VP16 in the construct with FUSN transformed VP16 into an activator that had similar potency to VPR. Notably, and similar to VPR, p65 and Rta, the activation capacity of PHR-GFP-VP16 did not depend on the actual formation of visible phase-separated droplets. Cells with and without droplets showed a similarly enhanced level of activation (**Fig. S3H**). We conclude that multivalent interactions increase activation capacity but that the additional formation of droplets has no effect on transcriptional activation. Moreover, certain types of droplets like those containing bridging factors can efficiently inhibit

transcription activation even though they increase the local TF concentration at the promoter.

TF residence times are determined by both the DBD and the AD

To establish a link between AD properties and TF binding we next compared the binding turnover of different TF constructs with high (VPR) or low (VP16) phase separation propensity by FRAP (**Fig. 4A, B, S4A-D**). Measurements were conducted for the four dCas9-based complex architectures, direct fusions of VP16 and VPR to rTetR and BLInCR rTetR (**Fig. 4C**). Mobility and interactions were determined at the reporter gene array as well as in other regions of the nucleus to compute normalized recovery curves that were fitted by a reaction-diffusion model for clustered binding sites. The effective diffusion coefficient, the dissociation rate k_{off} and the immobile fraction of stably bound molecules during the observation period of four minutes were determined (**Fig. S4E, Table S5**). Direct fusions to dCas9 displayed the slowest recovery, whereas tdPCP-GFP on the PP7-loops of the dCas9 exchanged within seconds. The light-induced interaction of PHR and CIBN led to recovery times comparable to tdPCP on PP7 for the respective VP16 or VPR fusions. For the loop, BLInCR-dCas9 and BLInCR-loop complexes recovery was substantially slowed down by VPR compared to VP16 (**Fig. 4C**). These observations suggest that the high self-interaction propensity of VPR stabilizes the binding of transiently bound complexes. For strongly bound dCas9 fusion complex this additionally recruited, indirectly bound fraction of molecules can be observed as an additional recovery term that is present for VPR but absent for VP16. The computed residence times ranged from τ_{res} = 12 ± 6 s for tdPCP-GFP on PP7 to τ_{res} being larger than the observation time of 240 s for dCas9-GFP-VP16 on the *lacO* sites (**Table S5, Fig. 4C**). Residence times for VPR as compared to VP16 of the loop, BLInCR and BLInCR-loop dCas9 complexes were consistently >14 s higher and the immobile fraction was increased by 2-7 %. For the AD fusion constructs with rTetR and dCas9, the VPR fusion displayed shorter values of τ_{res} and for the dCas9 fusion a strongly reduced immobile fraction compared to VP16 (**Table S5**). These differences between VP16 and VPR are likely to reflect an increased fraction of indirectly bound molecules for VPR that display a faster exchange than the protein fraction that is directly bound to DNA. To confirm that VPR complexes comprise an additional fraction of indirectly bound molecules, we compared the intensity of VPR and VP16 assemblies recruited via the loop configuration (**Fig. 4I**). We found a 1.9-fold higher spot intensity for tdPCP-GFP-VPR compared to tdPCP-GFP-VP16 (p = 0.0006, Welch two-sample t-test), confirming the additional recruitment seen in FRAP (**Fig. 4E**). We conclude that the apparent TF turnover rate and residence time does not only depend on the DBD but is significantly influenced by the AD as it mediates the binding of additional TF molecules to those that are bound to DNA directly and stabilizes the directly bound proteins. This enrichment of TFs via protein-protein interactions reflects the AD propensity to engage in multivalent interactions and was positively

linked to the observed optodroplets formation propensities for these two ADs.

Transcription activation can occur independent of BRD4 and H3K27ac

TFs initiate transcription via different mechanisms that include the assembly of the transcription machinery, catalyzing its transition into an active state as well as chromatin state changes that promote transcription (*41*). To reveal mechanistic differences between different TF complexes, we first compared their activity by quantitative real-time PCR (qRT-PCR) measurements of reporter RNA levels at 24 hours after induction (**Fig. 5A, Table S6**). In these experiments, the BLInCR-dCas9 and BLInCR-loop constructs failed to activate the core CMV promoter of the gene array although transcriptional activation by a BLInCR-dCas9 construct has been reported previously for the endogenous human *IL1RN* or *HBG1/2* promoters and to a lesser extent for *ASCL1* (*35*) (**Fig. S5A-C, Supplemental Information**). In contrast, all other TF complexes were able to activate transcription with VPR consistently being a stronger activator than VP16. Next, the steady-state nascent RNA levels together with enrichment of BRD4 and H3K27ac were determined by a fluorescence microscopy assay (**Fig. 5B, 5C**) and represented as normalized radial profiles across the gene array (**Fig. 5D**). This analysis revealed that VPR displayed stronger BRD4 and H3K27ac enrichment than VP16 except for the loop construct. Recruitment of the histone acetyltransferase p300 core domain fused to dCas9 resulted in deposition of H3K27ac and BRD4 accumulation. Notably, the transcriptionally inactive BLInCR-dCas9 and BLInCR-loop complexes were capable to induce enrichment of co-activation marks BRD4 and H3K27ac raising the possibility that this would be sufficient to activate other promoters like *IL1RN* or *HBG1/2* (*35*) (**Fig. 5D, Supplemental Information**). In summary, we conclude that direct transcription activation can occur in parallel to co-activator recruitment and histone acetylation and distinguish three different TF types: (i) Strong activators like dCas9-VPR and rTetR-VPR fusions that induce both transcription and high enrichments levels of BRD4 and H3K27ac. (ii) Activators like the rTetR-VP16 fusion that displayed moderate but robust activation at very low levels of BRD4 and H3K27ac. (iii) The dCas9 based BLInCR constructs with high turnover rate efficiently recruited BRD4 and induced H3K27ac but failed to activate the CMV core promoter.

VPR recruits BRD4 directly and is less dependent on pre-existing histone acetylation

We observed that both activating and non-activating PHR-GFP-VPR complexes sometimes enriched mCherry-BRD4 in optodroplets upon over-expression while this did not occur with PHR-GFP-VP16 (**Fig. 5E, 5F**). Thus, we hypothesized that transient multivalent interactions between VPR and BRD4 are part of the functional differences between VP16 and VPR. To test this possibility, we used the transcription-incompetent BLInCR-loop complex to monitor transcription-independent BRD4 binding after light-induced promoter recruitment of PHR-GFP-VP16 or -VPR (**Fig. 5G**). BRD4 accumulation was strong and fast for VPR with an initial steep

rise of the BRD4 levels over the first 10 minutes followed by a phase of slower BRD4 accumulation (**Fig. 5H-I**). VP16 did not display such biphasic kinetics. Next, we conducted the same experiment after pre-treating the cells with the inhibitor JQ1 that disrupts BRD4 interactions with acetylated histones to evaluate the contribution of BRD4 binding that is independent of acetylation. JQ1 pre-treatment completely abrogated BRD4 accumulation for VP16. For VPR the initial steep rise remained unaffected but BRD4 binding during the second phase was reduced (**Fig. 5I, right**). This observation suggests a direct VPR-BRD4 interaction that is followed by subsequent binding of BRD4 to acetylated histones via its bromodomain. JQ1 treatment did not reduce nascent RNA production induced by PHR-GFP-VP16/-VPR to CIBN-rTetR (**Fig. S5D, Table S7**). Bulk RNA levels were moderately reduced in the qRT-PCR assay only for VPR (1.8-fold reduction) but not for VP16 (1.1-fold reduction) (**Fig. S5E, Table S6**). We conclude that BRD4 accumulation accompanies transcriptional activation but is not essential for reporter gene induction. It may, however, enhance transcription activation by VPR or stabilize the activated state. Next, we assessed the contribution of histone acetylation to the activation capacity of both VP16 and VPR. A dCas9-GFP-p300core construct was constitutively recruited to the *lacO* sites to establish a locally hyper-acetylated state. Subsequently, light-induced transcription by binding of PHR-GFP-VP16 vs. PHR-GFP-VPR to CIBN-rTetR was quantified (**Fig. 5J**). VP16 displayed an enhanced transcriptional response in RNA production using qRT-PCR, which was absent for VPR (**Fig. 5K, Table S6**). When observing nascent RNA at the gene array by microscopy, a more pronounced increase of the plateau level was observed for VP16 (2.9-fold) than VPR (1.8-fold) while activation kinetics were similar (**Fig. S5G-I, Table S7**). We conclude that pre-existing histone acetylation can increase the transcriptional output and does so to a higher extent for VP16. Accordingly, the lower transcription activation capacity of VP16 could be related in part to its inability to directly bind histone acetylases like p300 as well as the BRD4 co-activator.

Shortened residence times reduces activation capacity

To test if TF residence time and transcriptional output are linked, we artificially increased the turnover of DNA bound dCas9 complexes at the promoter by introducing a mutation into the sgRNA targeting the *tetO* repeats (**Fig. 6A**). We analyzed 20 sgRNA mutants and selected the mutated sgRNA *tet*O-C2G (sgRNA-mut) for further studies and comparison with the wildtype sgRNA sequence (sgRNA-wt) (**Fig. S6A, Table S2**). A FRAP analysis revealed that the residence time of sgRNA-mut vs sgRNA-wt strongly decreased for dCas9-GFP-VPR from τ_{res} = 124 s (95 % CI: 75-347 s) to τ_{res} = 57 s (95 % CI: 34-184 s) (**Fig. 6B, Table S5**). In addition, the immobile fraction was lowered from 36 % to 7 % (95 % CIs: 25-47 % and 0-16 %). The two different sgRNAs allowed it to compare high (sgRNA-wt) and low (sgRNA-mut) residence times within the same activation complex architecture. For sgRNA-mut, occupancy

was reduced to 14 % (VP16) and 37 % (VPR) of the original value (**Fig. 6C, 6D**). The fraction of cells with visible dCas9 recruitment decreased from 90 % to 76 % (VPR) and from 59 % to 17 % (VP16) (**Fig. S6B, Table S8**) and bulk reporter RNA levels were strongly reduced for both VP16 and VPR (**Fig. 6E**). Furthermore, binding sites were no longer fully occupied with sgRNA-mut even at high dCas9-GFP-VPR expression levels (**Fig. S6C**). For sgRNA-wt a continuous increase of occupancy with activator expression was observed, which is likely to reflect an increase of indirectly recruited molecules via VPR-VPR interactions. As expected, RNA production increased with occupancy. In order to separate the effect of occupancy and residence time, we binned cells into groups with equal occupancy and compared their nascent RNA production. The average RNA production induced by VPR was consistently lower for short residence times with sgRNA-mut vs. sgRNA-wt within each group (**Fig. 6F**) (VPR: 2 - 6-fold, VP16: 1.3 - 2-fold; VPR: P<0.001, VP16: P>0.05, two-way ANOVA of occupancy group and sgRNA). We also measured the radial BRD4 and H3K27ac enrichment profiles and observed a robust enrichment even with reduced VPR residence times (**Fig. 6G**). This corroborates our previous findings that BRD4 recruitment and histone acetylation occur efficiently even at high AD turnover rate. The residence time dependency of activation suggests that the TF is involved in an energy-dependent step like a posttranslational modification of the transcription complex that is independent of histone acetylation/BRD4 accumulation. A kinetic model illustrates how the residence time of the TF in the bound state can become a key determinant of transcription output independent of binding site occupancy (**Fig. 6H, Supplemental Information**).

Discussion

We dissected the transcription activation process at a reporter gene array for a panel of TF constructs with diverse features and summarize the results in the scheme depicted in **Fig. 7**. We find that efficient transcription activation depends not only dependent on TF binding site occupancy but also requires a sufficiently long TF residence time. Thus, reactions between the TF binding step and the start of transcription are likely to involve a kinetic proofreading mechanism, as for example nucleosome remodeling (*13*) or ATP-dependent promoter DNA melting (*3*). It is noted that our analysis for the first time directly demonstrates how transcription activation strength is reduced with shorter residence time in an otherwise identical system and while maintaining the same degree of binding site occupancy. In this manner, we corroborate conclusions from previous studies on the importance of this parameter (*10-15*). In addition, we find that DBD and AD activities are linked and mutually affect TF binding and activation properties. For strongest activation, high-affinity DNA binding with long residence times at full site occupancy as well as multivalent interactions of the AD were needed. This state was

characterized by indirectly bound additional TF molecules, the recruitment of co-activators like BRD4 and the accumulation of H3K27ac. While all ADs were able to induce transcription, those with a high propensity for multivalent interactions as assessed via the optodroplet assay displayed faster and stronger activation and a larger fraction of responding cells. This effect did not depend on the actual formation of liquid droplets. Rather, we observed a trend towards slower activation when PHR-AD optodroplets assembled. Inducing droplet formation via addition of bridging factors had an inhibitory effect, possibly caused by the specific composition of the promoter-tethered assembly or as a result from sequestering components of the transcription machinery/co-factors into optodroplets located away from the target reporter array. Recent studies investigated the functional consequences of TF phase separation and reported that droplets formed by light induction of PHR/CRY2-TAF15 (*27*) or IDR-VP16 constructs (*28*) amplify gene expression or increase transcription activation. Furthermore, transcriptional condensates of super-enhancers have been proposed to drive transcription at highly active genes (*16, 19, 42, 43*). However, experiments that directly compare transcription activity of a chromatin bound activator in the presence/absence of droplet formation under identical conditions are lacking in these studies. Rather PHR fusions with light-induced association were compared to the dark state where they show reduced multivalency or an IDR was removed or added. This type of comparison provides valuable insight into the relation between TF interaction properties and transcription regulation. However, it does not distinguish between the effect of increasing multivalent interactions of a given TF and the actual formation of phase separated liquid droplets. Here, we demonstrate that it is not justified to generally assume that liquid activator droplets at the promoter would enhance transcription as we see a neutral or an inhibitory effect. It remains to be demonstrated whether the formation of inhibitory transcriptional condensates can occur in an endogenous cellular environment, for example to establish refractory promoter states (*44*). It is noted, that repression of RNA Pol I repression has been reported in the phase-separated nucleolar cap (*45*). Furthermore, our experiments indicate that the ability of TFs to form liquid droplets under certain conditions (e.g., by promoting their formation in PHR fusions) reflects the propensity of the AD to engage in multivalent interactions that are functionally relevant without an LLPS process. This conclusion is supported by findings of Chong et al. who report that local transient multivalent interactions of TFs at physiological concentrations induce binding and transcription, but that LLPS requires gross TF over-expression (*43*). We observed a boost in transcriptional activation when increasing the self-interaction propensity of PHR-VP16 by fusing it to the N-terminal IDR of FUS. This effect was again independent of optodroplet formation. Thus, non-phase separated chromatin binding and interactions with histone acetyl transferases and BRD4 are enhanced by TF multivalency and can provide the highest level of transcription activation in the absence of LLPS. As previously reported BRD4 displays transient multivalent interactions (*42, 46, 47*)

that are likely to drive direct binding to VPR and to maintain enrichment of BRD4 upon weakened DNA binding by the sgRNA mutation. It is noted that BRD4 was neither required nor sufficient to induce transcription in our experiments. Furthermore, transcription was not a prerequisite for BRD4 or H3K27 histone acetylation. We conclude that robust transcriptional induction requires the stable binding of the AD at the promoter for interactions with the core transcriptional machinery, while co-activators can also be recruited to the promoter by TFs at high turnover rate of the bound state. Thus, co-activators and H3K27ac act independently of forming a transcriptional-competent Pol II complex in our system and could boost transcriptional activation or increase the persistence of the activated state. In summary, our study reveals how the interplay between DNA binding site occupancy, residence time, multivalent AD interactions, BRD4 co-activator recruitment and histone acetylation as well as liquid droplet formation determine the transcription activation capacity of a TF. They provide novel insights into how transitions between active and inactive promoter states can be regulated. Furthermore, we anticipate that our findings will inform approaches that apply CRISPR/dCas9 based synthetic transcription factors to control gene expression programs (*48*).

Author contributions

Study design: JT, LF, KR. Acquisition of data: JT, LF, AR, PG. Analysis of data: all authors; Drafting of manuscript: JT, LF, KR. Manuscript reviewing: all authors. Supervision and coordination: KR

Acknowledgements

References

1. V. Haberle, A. Stark, Eukaryotic core promoters and the functional basis of transcription initiation. *Nat Rev Mol Cell Biol* **19**, 621-637 (2018).
2. R. Andersson, A. Sandelin, Determinants of enhancer and promoter activities of regulatory elements. *Nat Rev Genet* **21**, 71-87 (2020).
3. S. Osman, P. Cramer, Structural Biology of RNA Polymerase II Transcription: 20 Years On. *Annu Rev Cell Dev Biol* **36**, 1-34 (2020).

4. A. D. Frankel, P. S. Kim, Modular structure of transcription factors: implications for gene regulation. *Cell* **65**, 717-719 (1991).

5. M. V. Staller, A. S. Holehouse, D. Swain-Lenz, R. K. Das, R. V. Pappu, B. A. Cohen, A High-Throughput Mutational Scan of an Intrinsically Disordered Acidic Transcriptional Activation Domain. *Cell Syst* **6**, 444-455 e446 (2018).

6. I. Sadowski, J. Ma, S. Triezenberg, M. Ptashne, GAL4-VP16 is an unusually potent transcriptional activator. *Nature* **335**, 563-564 (1988).

7. R. Brent, M. Ptashne, A eukaryotic transcriptional activator bearing the DNA specificity of a prokaryotic repressor. *Cell* **43**, 729-736 (1985).

8. A. Chavez, J. Scheiman, S. Vora, B. W. Pruitt, M. Tuttle, P. R. I. E, S. Lin, S. Kiani, C. D. Guzman, D. J. Wiegand, D. Ter-Ovanesyan, J. L. Braff, N. Davidsohn, B. E. Housden, N. Perrimon, R. Weiss, J. Aach, J. J. Collins, G. M. Church, Highly efficient Cas9-mediated transcriptional programming. *Nat Methods* **12**, 326-328 (2015).

9. L. Bintu, N. E. Buchler, H. G. Garcia, U. Gerland, T. Hwa, J. Kondev, R. Phillips, Transcriptional regulation by the numbers: models. *Curr Opin Genet Dev* **15**, 116-124 (2005).

10. K. Clauss, A. P. Popp, L. Schulze, J. Hettich, M. Reisser, L. Escoter Torres, N. H. Uhlenhaut, J. C. M. Gebhardt, DNA residence time is a regulatory factor of transcription repression. *Nucleic Acids Res* **45**, 11121-11130 (2017).

11. A. Loffreda, E. Jacchetti, S. Antunes, P. Rainone, T. Daniele, T. Morisaki, M. E. Bianchi, C. Tacchetti, D. Mazza, Live-cell p53 single-molecule binding is modulated by C-terminal acetylation and correlates with transcriptional activity. *Nat Commun* **8**, 313 (2017).

12. I. Brouwer, T. L. Lenstra, Visualizing transcription: key to understanding gene expression dynamics. *Curr Opin Chem Biol* **51**, 122-129 (2019).

13. R. Shelansky, H. Boeger, Nucleosomal proofreading of activator-promoter interactions. *Proc Natl Acad Sci U S A* **117**, 2456-2461 (2020).

14. A. Callegari, C. Sieben, A. Benke, D. M. Suter, B. Fierz, D. Mazza, S. Manley, Single-molecule dynamics and genome-wide transcriptomics reveal that NF-kB (p65)-DNA binding times can be decoupled from transcriptional activation. *PLoS Genet* **15**, e1007891 (2019).

15. J. B. Gurdon, K. Javed, M. Vodnala, N. Garrett, Long-term association of a transcription factor with its chromatin binding site can stabilize gene expression and cell fate commitment. *Proc Natl Acad Sci U S A* **117**, 15075-15084 (2020).

16. D. Hnisz, K. Shrinivas, R. A. Young, A. K. Chakraborty, P. A. Sharp, A Phase Separation Model for Transcriptional Control. *Cell* **169**, 13-23 (2017).

17. K. Shrinivas, B. R. Sabari, E. L. Coffey, I. A. Klein, A. Boija, A. V. Zamudio, J. Schuijers, N. M. Hannett, P. A. Sharp, R. A. Young, A. K. Chakraborty, Enhancer Features that Drive Formation of Transcriptional Condensates. *Mol Cell* **75**, 549-561 e547 (2019).

18. L. Frank, K. Rippe, Repetitive RNAs as Regulators of Chromatin-Associated Subcompartment Formation by Phase Separation. *J Mol Biol* **432**, 4270-4286 (2020).

19. B. R. Sabari, A. Dall'Agnese, R. A. Young, Biomolecular Condensates in the Nucleus. *Trends Biochem Sci* **45**, 961-977 (2020).

20. P. Quintero-Cadena, T. L. Lenstra, P. W. Sternberg, RNA Pol II Length and Disorder Enable Cooperative Scaling of Transcriptional Bursting. *Mol Cell* **79**, 207-220 e208 (2020).

21. S. C. Weber, C. P. Brangwynne, Getting RNA and protein in phase. *Cell* **149**, 1188-1191 (2012).

22. V. N. Uversky, I. M. Kuznetsova, K. K. Turoverov, B. Zaslavsky, Intrinsically disordered proteins as crucial constituents of cellular aqueous two phase systems and coacervates. *FEBS Lett* **589**, 15-22 (2015).

23. S. F. Banani, H. O. Lee, A. A. Hyman, M. K. Rosen, Biomolecular condensates: organizers of cellular biochemistry. *Nat Rev Mol Cell Biol* **18**, 285-298 (2017).

24. A. Drino, M. R. Schaefer, RNAs, Phase Separation, and Membrane-Less Organelles: Are Post-Transcriptional Modifications Modulating Organelle Dynamics? *Bioessays* **40**,

e1800085 (2018).

25. S. Kent, K. Brown, C. H. Yang, N. Alsaihati, C. Tian, H. Wang, X. Ren, Phase-Separated Transcriptional Condensates Accelerate Target-Search Process Revealed by Live-Cell Single-Molecule Imaging. *Cell Rep* **33**, 108248 (2020).

26. S. Brodsky, T. Jana, K. Mittelman, M. Chapal, D. K. Kumar, M. Carmi, N. Barkai, Intrinsically Disordered Regions Direct Transcription Factor In Vivo Binding Specificity. *Mol Cell* **79**, 459-471 e454 (2020).

27. M. T. Wei, Y. C. Chang, S. F. Shimobayashi, Y. Shin, A. R. Strom, C. P. Brangwynne, Nucleated transcriptional condensates amplify gene expression. *Nat Cell Biol* **22**, 1187-1196 (2020).

28. N. Schneider, F.-G. Wieland, D. Kong, A. A. M. Fischer, M. Hörner, J. Timmer, H. Ye, W. Weber, Liquid-liquid phase separation of light-inducible transcription factors increases transcription activation in mammalian cells and mice. *Science Advances* **7**, (2021).

29. F. Erdel, K. Rippe, Formation of chromatin subcompartments by phase separation. *Biophys J* **114**, 2262-2270 (2018).

30. D. T. McSwiggen, M. Mir, X. Darzacq, R. Tjian, Evaluating phase separation in live cells: diagnosis, caveats, and functional consequences. *Genes Dev* **33**, 1619-1634 (2019).

31. D. T. McSwiggen, A. S. Hansen, S. S. Teves, H. Marie-Nelly, Y. Hao, A. B. Heckert, K. K. Umemoto, C. Dugast-Darzacq, R. Tjian, X. Darzacq, Evidence for DNA-mediated nuclear compartmentalization distinct from phase separation. *Elife* **8**, (2019).

32. F. Erdel, A. Rademacher, R. Vlijm, J. Tunnermann, L. Frank, R. Weinmann, E. Schweigert, K. Yserentant, J. Hummert, C. Bauer, S. Schumacher, A. Al Alwash, C. Normand, D. P. Herten, J. Engelhardt, K. Rippe, Mouse Heterochromatin Adopts Digital Compaction States without Showing Hallmarks of HP1-Driven Liquid-Liquid Phase Separation. *Mol Cell* **78**, 236-249 e237 (2020).

33. M. J. Kennedy, R. M. Hughes, L. A. Peteya, J. W. Schwartz, M. D. Ehlers, C. L. Tucker, Rapid blue-light-mediated induction of protein interactions in living cells. *Nat Methods* **7**, 973-975 (2010).

34. A. Rademacher, F. Erdel, J. Trojanowski, S. Schumacher, K. Rippe, Real-time observation of light-controlled transcription in living cells. *J Cell Sci* **130**, 4213-4224 (2017).

35. L. R. Polstein, C. A. Gersbach, A light-inducible CRISPR-Cas9 system for control of endogenous gene activation. *Nat Chem Biol* **11**, 198-200 (2015).

36. S. M. Janicki, T. Tsukamoto, S. E. Salghetti, W. P. Tansey, R. Sachidanandam, K. V. Prasanth, T. Ried, Y. Shav-Tal, E. Bertrand, R. H. Singer, D. L. Spector, From silencing to gene expression: real-time analysis in single cells. *Cell* **116**, 683-698 (2004).

37. N. Gustafsson, S. Culley, G. Ashdown, D. M. Owen, P. M. Pereira, R. Henriques, Fast live-cell conventional fluorophore nanoscopy with ImageJ through super-resolution radial fluctuations. *Nat Commun* **7**, 12471 (2016).

38. Y. Shin, J. Berry, N. Pannucci, M. P. Haataja, J. E. Toettcher, C. P. Brangwynne, Spatiotemporal Control of Intracellular Phase Transitions Using Light-Activated optoDroplets. *Cell* **168**, 159-171 e114 (2017).

39. M. Lewis, G. Chang, N. C. Horton, M. A. Kercher, H. C. Pace, M. A. Schumacher, R. G. Brennan, P. Lu, Crystal structure of the lactose operon repressor and its complexes with DNA and inducer. *Science* **271**, 1247-1254 (1996).

40. A. Patel, H. O. Lee, L. Jawerth, S. Maharana, M. Jahnel, M. Y. Hein, S. Stoynov, J. Mahamid, S. Saha, T. M. Franzmann, A. Pozniakovski, I. Poser, N. Maghelli, L. A. Royer, M. Weigert, E. W. Myers, S. Grill, D. Drechsel, A. A. Hyman, S. Alberti, A Liquid-to-Solid Phase Transition of the ALS Protein FUS Accelerated by Disease Mutation. *Cell* **162**, 1066-1077 (2015).

41. T. I. Lee, R. A. Young, Transcription of eukaryotic protein-coding genes. *Annu Rev Genet* **34**, 77-137 (2000).

42. B. R. Sabari, A. Dall'Agnese, A. Boija, I. A. Klein, E. L. Coffey, K. Shrinivas, B. J. Abraham, N. M. Hannett, A. V. Zamudio, J. C. Manteiga, C. H. Li, Y. E. Guo, D. S. Day, J. Schuijers,

E. Vasile, S. Malik, D. Hnisz, T. I. Lee, Cisse, II, R. G. Roeder, P. A. Sharp, A. K. Chakraborty, R. A. Young, Coactivator condensation at super-enhancers links phase separation and gene control. *Science* **361**, eaar3958-3917 (2018).

43. S. Chong, C. Dugast-Darzacq, Z. Liu, P. Dong, G. M. Dailey, C. Cattoglio, A. Heckert, S. Banala, L. Lavis, X. Darzacq, R. Tjian, Imaging dynamic and selective low-complexity domain interactions that control gene transcription. *Science* **361**, eaar2555-2517 (2018).

44. C. Li, F. Cesbron, M. Oehler, M. Brunner, T. Hofer, Frequency Modulation of Transcriptional Bursting Enables Sensitive and Rapid Gene Regulation. *Cell Syst* **6**, 409-423 e411 (2018).

45. S. Ide, R. Imai, H. Ochi, K. Maeshima, Transcriptional suppression of ribosomal DNA with phase separation. *Sci Adv* **6**, (2020).

46. W. K. Cho, J. H. Spille, M. Hecht, C. Lee, C. Li, V. Grube, Cisse, II, Mediator and RNA polymerase II clusters associate in transcription-dependent condensates. *Science* **361**, 412-415 (2018).

47. X. Han, D. Yu, R. Gu, Y. Jia, Q. Wang, A. Jaganathan, X. Yang, M. Yu, N. Babault, C. Zhao, H. Yi, Q. Zhang, M. M. Zhou, L. Zeng, Roles of the BRD4 short isoform in phase separation and active gene transcription. *Nat Struct Mol Biol* **27**, 333-341 (2020).

48. M. Pandelakis, E. Delgado, M. R. Ebrahimkhani, CRISPR-Based Synthetic Transcription Factors In Vivo: The Future of Therapeutic Cellular Programming. *Cell Syst* **10**, 1-14 (2020).

49. J. G. Zalatan, M. E. Lee, R. Almeida, L. A. Gilbert, E. H. Whitehead, M. La Russa, J. C. Tsai, J. S. Weissman, J. E. Dueber, L. S. Qi, W. A. Lim, Engineering complex synthetic transcriptional programs with CRISPR RNA scaffolds. *Cell* **160**, 339-350 (2015).

50. K. Gunther, M. Rust, J. Leers, T. Boettger, M. Scharfe, M. Jarek, M. Bartkuhn, R. Renkawitz, Differential roles for MBD2 and MBD3 at methylated CpG islands, active promoters and binding to exon sequences. *Nucleic Acids Res* **41**, 3010-3021 (2013).

51. T. Frahm, H. Hauser, M. Koster, IFN-type-I-mediated signaling is regulated by modulation of STAT2 nuclear export. *J Cell Sci* **119**, 1092-1104 (2006).

52. I. F. Lau, S. R. Filipe, B. Soballe, O. A. Okstad, F. X. Barre, D. J. Sherratt, Spatial and temporal organization of replicating Escherichia coli chromosomes. *Mol Microbiol* **49**, 731-743 (2003).

53. T. Pankert, T. Jegou, M. Caudron-Herger, K. Rippe, Tethering RNA to chromatin for fluorescence microscopy based analysis of nuclear organization. *Methods* **123**, 89-101 (2017).

54. U. Rothbauer, K. Zolghadr, S. Muyldermans, A. Schepers, M. C. Cardoso, H. Leonhardt, A versatile nanotrap for biochemical and functional studies with fluorescent fusion proteins. *Mol Cell Proteomics* **7**, 282-289 (2008).

55. K. Muller-Ott, F. Erdel, A. Matveeva, J. P. Mallm, A. Rademacher, M. Hahn, C. Bauer, Q. Zhang, S. Kaltofen, G. Schotta, T. Hofer, K. Rippe, Specificity, propagation, and memory of pericentric heterochromatin. *Mol Syst Biol* **10**, 746 (2014).

56. J. Trojanowski, A. Rademacher, F. Erdel, K. Rippe, in *Imaging Gene Expression: Methods and Protocols, Methods in Molecular Biology, vol. 2028,* Y. Shav-Tal, Ed. (Springer Nature, New York, 2019), pp. 251-270.

57. B. L. Sprague, F. Muller, R. L. Pego, P. M. Bungay, D. A. Stavreva, J. G. McNally, Analysis of binding at a single spatially localized cluster of binding sites by fluorescence recovery after photobleaching. *Biophys J* **91**, 1169-1191 (2006).

58. J. Schindelin, I. Arganda-Carreras, E. Frise, V. Kaynig, M. Longair, T. Pietzsch, S. Preibisch, C. Rueden, S. Saalfeld, B. Schmid, J. Y. Tinevez, D. J. White, V. Hartenstein, K. Eliceiri, P. Tomancak, A. Cardona, Fiji: an open-source platform for biological-image analysis. *Nat Methods* **9**, 676-682 (2012).

Materials and Methods

Plasmids

Plasmids and sgRNA sequences are listed in **Supplemental Table S1 and S2**. Protein constructs were expressed under control of a CMV promoter using pEGFP-C1/N1 (Clontech) (enhanced GFP, referred to here as GFP) or pcDNA3.1 (Invitrogen) vector backbones. Plasmids expressing *lacO/tetO* targeting sgRNAs with 2xPP7 loops were designed as gBlocks (Integrated DNA Technology) and cloned into a U6 promoter-driven sgRNA expression vector derived from Addgene plasmid #61424. The PP7 loop sequence used in this study was adapted from Zalatan et al., 2015 (*49*). The dCas9 open reading frame used in all dCas9-based constructs originates from Addgene plasmid #60910. Activation domains were obtained from Addgene plasmid #63798 (VPR, p65, Rta) (*8*), Addgene plasmid #103836 (VP16) (*50*) and pSTAT2-EGFP (STAT2, amino acids 1-10 and 722-857) (*51*). The p300 core histone acetyltransferase domain was derived from Addgene plasmid #61357. CRY2PHR and CIBN domains were taken from Addgene plasmid #26866 and #26867, respectively. The CIBN-dCas9-CIBN expression construct corresponds to Addgene plasmid #60553. Tandem MCP with tandem Tomato (tdMCP-tdTomato) was derived from Addgene plasmids #40649 and #54642. The TATA-box of the promoter was removed to reduce expression levels. The tandem PCP (tdPCP) protein was derived from Addgene plasmid #40650. LacI and TetR constructs are based on the fluorescently tagged proteins described by Lau et al., 2003 (*52*) and Pankert et al., 2017 (*53*). The rTetR protein sequence was subcloned from the Tet-On transactivator used in the commercially available Tet-On 3G system (Takara Bio). FUSN was derived from Addgene #122148. GBP was derived from Rothbauer et al, 2008 (*54*).

Cell Culture

U2OS 2-6-3 cells containing the stably integrated *lacO/tetO* reporter gene cluster (*36*) were grown in DMEM (1 g/l glucose, Gibco) without phenol-red supplemented with 10 % tetracycline-free fetal calf serum (FCS), penicillin/streptomycin and 2 mM L-glutamine using standard cell culture methods at 37 °C and 5 % CO_2. Cells were seeded onto 8-well chambered coverglass slides (Nunc Labtek, Thermo Fisher Scientific) at a density of $2 \cdot 10^4$ cells per well. For qRT-PCR $3 \cdot 10^5$ cells were seeded in 6-well plates. One day after seeding, the medium was replaced with imaging medium (FluoroBrite, Gibco, A1896701; 10 % tet-free FCS; penicillin/streptomycin; 2 mM L-glutamine) and cells were transfected using the Xtreme-Gene 9 reagent (Roche) according to the manufacturer's guidelines. Briefly, 200-400 ng plasmid DNA and 0.6 µl transfection reagent in 20 µl OptiMem (Gibco) were used per well for microscopy experiments. The plasmid DNA mix consisted of 100 ng of guide RNA plasmid and 100 ng of equal amounts of the remaining constructs. For transfections without guide RNA plasmid the 200 ng were split equally among the plasmids. Transfection reactions were scaled

up to 2 µg plasmid DNA per well for qRT-PCR experiments. Cells were protected from light until the start of experiments for FRAP and induction time course experiments with light-responsive constructs. FRAP experiments were conducted 48 hours post-transfection, all the other experiments 24 hours post-transfection. For the radial profile microscopy experiments or qRT-PCR of light-inducible activator constructs, cells were illuminated by diffuse white LED light for 24 hours. rTetR activator constructs were allowed to bind in presence of 5 µg/mL doxycycline (Sigma-Aldrich, D9891) which was added after transfection.

RNA isolation and qRT-PCR

Total RNA was isolated using QIAzol lysis reagent (Qiagen), followed by one round of chloroform extraction and isopropanol precipitation. The purified RNA was treated for 30 min at 37°C with RQ1 DNase (Promega) according to the manufacturer's protocol and then purified using one round of each phenol/chloroform and chloroform extraction followed by precipitation using ethanol in presence of 300 mM sodium acetate pH 5.5 and GlycoBlue coprecipitant (Thermo Fisher Scientific). RNA concentration and purity were determined by absorbance measurement. Per sample, one microgram of DNase-treated RNA was used as input for cDNA synthesis using the Superscript IV reverse transcriptase protocol (Thermo Fisher Scientific). qRT-PCR was carried out in technical triplicates with 2 µl of 1:40-diluted cDNA per 10 µl reaction using SYBR Green PCR Mastermix (Applied Biosystems) with a final primer concentration of 500 nM. The following PCR primers (Eurofins Genomics) were used. Human beta-actin fwd: 5'-TCC CTG GAG AAG AGC TAC GA-3', rev: 5'-AGC ACT GTG TTG GCG TAC AG-3'; VPR-VP16 fwd: 5'- AAGAAGAGGAAGGTTGCCCC-3', rev: 5'-CCC CAG GCT GAC ATC GGT-3'; CFP-SKL fwd: 5'-GTCCGGACTCAGATCTCGA-3', rev: 5'-TTC AAA GCT TGG ACT GCA GG-3'. The qRT-PCR analysis was carried out using the $2^{-\Delta\Delta CT}$ method. Reporter RNA expression levels (CFP-SKL) were normalized to beta-actin mRNA levels (ΔCT) and then expressed as fold-change of the mock control.

Microscopy instrumentation

SRRF images and data for radial profiles and occupancy were acquired with an Andor Dragonfly 505 spinning disc microscope equipped with the Nikon Ti2-E inverted microscope and a 40x oil immersion objective (CFI Plan-Fluor 40x Oil 1.30/0.20, Nikon). Multicolor images were acquired using laser lines at 405 nm (tagBFP), 488 nm (GFP), 561 nm (tdTomato and mCherry) and 637 nm (Alexa 633) for excitation with a quad-band dichroic unit (405, 488, 561, 640 nm) and corresponding emission filters of 450/50 (tagBFP), 525/50 (GFP), 600/50 (tdTomato, mCherry) and 700/75 nm (Alexa 633) and an iXon Ultra 888 EM-CCD camera. Live cell experiments were conducted in an incubation chamber (Okolab) at 5 % CO_2 and 37 °C temperature. Light-induced time course and FRAP experiments were carried out with an AxioObserver Z1 widefield microscope (Zeiss) equipped with a 20x air objective (Zeiss Plan-

Apochromat 20x/0.8 M27), the Zen 2012 pro software including modules for z-stack, time-lapse and multi-position acquisition and an AxioCam MRm Rev.3 monochrome camera with filter sets with excitation bandpass, beam splitter, emission bandpass wavelength: GFP, 470/40 nm, 495 nm, 525/50 nm; tdTomato, 535/30 nm, 570 nm, 572/25 nm and mCherry, 550/25 nm, 590 nm, 629/62 nm. For spot bleaching at 473 nm in FRAP experiments the microscope was extended with an UGA40 70 mW laser scanning system (Rapp OptoElectronic). A Leica TCS SP5 II confocal microscope (Leica) equipped with a 63x Plan-Apochromat oil immersion objective was used for additional FRAP experiments as described previously (*55*) and for measuring recruitment/dissociation kinetics (**Supplemental Information**).

Super-resolution radial fluctuations (**SRRF**) **imaging of reporter locus**

Cells were transfected with LacI containing a SNAP-tag and the respective components of the activation complex directed to the *tetO* sites. After 24 hours SNAP-Cell 647-SiR substrate (New England Biolabs) was added to the medium at a concentration of 3 μM, incubated for 30 min and washed three times with medium, incubated with medium for 30 min and washed three times with PBS. Cells were fixed with 4 % paraformaldehyde for 10 min and washed once with PBS before imaging. Imaging was performed on the Andor Dragonfly spinning disc microscope with a 100x silicon immersion objective (CFI SR HP Apochromat Lambda S 100x, Nikon) and a 2x magnification lens to ensure oversampling. 200 frames were acquired per channel for one super-resolved SRRF image. Exposure time was 2.5 ms with 100 % laser intensity of the 488 nm or 637 nm laser for GFP or 647-SiR, respectively. SRRF analysis was performed using the SRRF-stream tool implemented in the microscope software with 5 x 5 sub-pixels, a ring radius of 1.5 pixels for radiality calculations and mean-projection of radiality images.

Light-induced time course experiments

Light-induced time course experiments followed the protocol given in (*56*) and were conducted with the AxioObserver Z1 widefield microscope. Slides with transfected cells were kept in the dark until the start of image acquisition and red-light illumination was used during sample preparation before initiating the reaction with blue light. For JQ1 (Sigma-Aldrich, SML1524) treatment the drug was diluted in medium and added to the respective wells to a final concentration of 1 µM three hours before the start of imaging. Doxycycline (Sigma-Aldrich, D9891) was added 15 minutes before imaging to a final concentration of 5 µg/ml in the dark to induce binding of CIBN-rTetR. The focal plane was determined by red-filtered transmitted light and kept constant by the hardware autofocus. Imaging time courses comprised repeated cycles of imaging of a grid of 16 positions (4x4, 50 % negative overlap) with three z-slices (distance 1.0 µm) in intervals of 2 minutes over 90 minutes or 60 minutes for BRD4 recruitment

experiments. After each time course experiment the slide was exchanged with a slide that had been stored in the dark to ensure that between experiments PHR molecules that had been exposed to stray light from a neighboring well had reverted to their inactive conformation in the dark.

Analysis of time course images

Image were processed with the EBImage and NSSQ R packages as described previously (*56*). In a first step positions of nuclei with successful recruitment of PHR-GFP-AD were manually selected and segmented in the GFP channel by automated local thresholding for each time point. The nucleus was tracked by mapping the segmented objects with minimal distance in consecutive frames. The best focal plane was selected from the z-stack for each time point using the intensity gradient inside the nucleus area. The reporter gene cluster was segmented inside the nuclear area using a quantile-based threshold in the PHR-GFP-AD channel. The spot position was tracked through the time course by finding the closest segmented object in consecutive images. The areas of spot (A_{spot}) and nucleus masks ($A_{nucleus}$) and the average intensities inside the spot (I_{spot}), nucleus ($I_{nucleus}$) and ring-shaped background regions around them (I_{spotbg}, $I_{nucleusbg}$) were measured in each channel. The amount of fluorescence intensity recruited to the reporter spot was then calculated as the product of background subtracted spot intensity and area:

$$I_{enriched}(t) = (I_{spot} - I_{spotbg}) \cdot A_{spot}$$

Segmented image series were manually curated by removing cells with morphological abnormalities, missing expression or segmentation errors and then classified as responders or non-responders based on visible accumulation of intensity in the reporter spot in the reader channel. In order to account for the small time shift of acquisition between positions in one imaging cycle, the intensity values at the beginning of each cycle were calculated by linear interpolation. The resulting single cell time courses were then either directly averaged for each time point to yield absolute intensity values or normalized by subtracting the initial value and dividing by the maximum value before averaging:

$$I_{norm}(t) = (I_{enriched}(t) - I_{enriched}(0))/max(I_{enriched}(t) - I_{enriched}(0))$$

Averaging was performed either for all cells or only for responder cells. The first value was subtracted so that all curves started at an intensity value of zero. For BRD4 recruitment time courses time traces were normalized to their maximum values without subtraction of the first time point. The value of the first time point was then subtracted after averaging. Times to half-activation were determined from single cell time courses as the first time point, at which the normalized intensity equaled or exceeded 0.5. The responder fraction was calculated as the number of cells annotated as responders divided by the total number of cells remaining after

manual curation. Time course maximum values were determined as the average plateau value of tdMCP-tdTomato intensity over the last five time points.

Light induced optodroplet formation

Image series of cells transfected with combinations of PHR-GFP-AD and CIBN-rTetR, CIBN-dCas9-CIBN or dCas9 + tdPCP-CIBN were acquired in the GFP channel with the same settings as the induction time course experiments over 6 cycles at 25 positions. For conditions with CIBN-rTetR doxycycline was added 15 minutes before imaging. All images were acquired in a single microscopy session and processed as described above. To remove the contribution of the reporter array spot to the nuclear intensity variation, the reporter spot was selected manually and removed from the nucleus mask using a disc shaped area with 7 pixels diameter. Mean and standard deviation of intensities in the processed nucleus images and in a ring-shaped background area around the nucleus were determined. Subsequently, image series were manually curated and classified as containing optodroplets or not by checking for the presence of spherical structures outside the reporter spot. The coefficient of variation (CV) of the nuclear intensity was used as a measure of droplet abundance and calculated as the ratio of standard deviation and mean of the nuclear intensity. The critical value for droplet formation was determined as the nuclear intensity at which the CV of the nuclear intensity exceeded an empirically determined threshold of 0.25. This threshold was selected, so that it yielded a good separation of cells manually annotated as droplet containing or not. In order to represent the CV as a smooth function of the nuclear intensity we fitted a logistic function to it:

$$D(c) = A + B / (1 + exp(-k \cdot (c - c_0))),$$

where *D(c)* is the droplet abundance, *c* the nuclear concentration and the remaining free fitting parameters are offset *A* and amplitude *B*. The intensity at which this function crosses 0.25 corresponds to the critical value.

FRAP analysis

FRAP experiments were carried out on the Zeiss widefield microscope described above with an external micromanipulation laser for bleaching. This set-up allowed fast acquisition of time courses in a large number of cells and conditions and yielded results similar to those obtained with a confocal microscope (**Fig. S4 A-C, Supplemental Information**). Laser position calibration was performed according to the UGA40 software instructions on a fluorescent calibration slide. Conditions with optogenetic constructs were illuminated for at least one minute in the GFP channel to saturate binding to CIBN before carrying out FRAP. The reporter spot was manually selected as bleach region and bleached at 100 % laser intensity for one second, 3-4 frames after starting an imaging time series of four minutes with one second intervals (on-spot bleach). For determining construct-specific diffusion coefficients a central

nuclear bleach region outside of the reporter spot was bleached and fluorescence recovery was monitored at 300 ms intervals for one minute (off-spot bleach). FRAP of *tetO*-bound dCas9-GFP-VPR with sgRNA-wt and sgRNA-mut was carried out with the same settings but with an alpha Plan-Apochromat 100x/1.46 Oil DIC M27 objective (Zeiss). The spot or bleach region intensities in the image series were quantified by a semi-automated analysis pipeline with our *R* software package *NSQFRAP* and normalized to pre-bleach and nuclear intensity to account for bulk bleaching. Normalized recovery curves were fitted with a reaction-diffusion model for clustered binding sites (*57*) using the empirical post-bleach profile as an initial condition and the effective diffusion coefficient determined from the off-spot FRAP measurements (**Fig. S4D, Supplemental Information**).

Analysis of binding and dissociation kinetics

Binding and dissociation time courses of PHR-mCherry-VP16 on CIBN constructs were performed on a Leica SP5 confocal microscope. Transfected cells were imaged using a 594 nm laser line (mCherry) for focusing without triggering the optogenetic components. An image was taken before starting a 2-3 min image series using both the 594 nm and 488 nm laser line for imaging the co-transfected GFP-LacI array marker and triggering PHR-CIBN interaction with time intervals of 6 seconds. After recoding this time series, the 488 nm laser line was switched off and 2 µm z-stacks (0.5 µm step-size) of the same positions were recorded for 20-30 min at 1 min intervals to monitor PHR-CIBN dissociation. Reporter spot tracking and intensity quantification were performed as described for FRAP and using the GFP-LacI array marker to identify the reporter spot. Spot intensities were subtracted from the background intensity determined in a ring-shaped area around the spot and normalized for each cell to the last (t = 168 s, binding) or first timepoint (t = 0 s, dissociation), respectively.

Immunofluorescence

Slide wells with transfected cells that had been illuminated for 24 hours were washed once with phosphate-buffered saline (PBS) and fixed with 4 % paraformaldehyde in PBS (Sigma-Aldrich, 252549) for 12 minutes. After washing with PBS cells were permeabilized with ice-cold 0.1 Triton-X100 (Merck, 108643) in PBS for 5 minutes. Blocking with 10 % goat serum (Cell Signaling Technology) in PBS for 15 minutes was followed by incubation with rabbit anti H3K27ac antibody (ab4729, Abcam, Lot GR183922-1, 1:1000) in 10 % goat serum for one hour at room temperature. Cells were washed three times for 5 min with 0.002 % NP40 (Sigma-Aldrich, i8896) in PBS. Incubation with the secondary antibody goat anti-rabbit Alexa 633 (Thermo Fisher Scientific, A21071, Lot 1073053, 1:1000) was done for 30 minutes at room temperature in 10 % goat serum/PBS. Cells were washed twice for 5 min with PBS and stored in PBS at 4 °C until they were imaged on the following day.

Single molecule RNA FISH

Probes of the RNAScope system (ACD Bio) against the MS2 sequence of the U2OS-2-6-3 reporter cell line covering position 851 to 2163 of the reporter RNA were custom designed by ACD Bio. Slides with transfected cells that had been illuminated for 24 hours were washed once with phosphate-buffered saline (PBS) and fixed with 4 % paraformaldehyde in PBS (Sigma-Aldrich, 252549) for 12 minutes. After washing three times with PBS cells were treated with 3 % hydrogen peroxide for five minutes, washed with PBS and treated with protease III (ACD Bio) diluted 1:15 for ten minutes, followed by three PBS washes. Hybridization of target and amplification probes was then performed according to the manufacturer's protocol. Target probes after amplification were labelled with Alexa Fluor 488 using the C1 detection kit. Cells were stored and imaged in PBS.

Spinning disc confocal microscopy for radial profiles and occupancy plots

Cells transfected with light-responsive constructs were cultured for 24 hours in the presence of diffuse white LED light after transfection and then subjected to imaging. For each condition 14 μm z-scans (1 μm step size) on at least 81 positions (9 x 9 grid, 1 % overlap) were recorded per slide well on an Andor Dragonfly 505 spinning disc microscope. Images were processed with the *NSSQ* package (*56*). Nuclei with activator recruitment in the GFP-AD channel or array marker signal were manually selected in maximum projections of each position and then segmented in sum-projected images by local thresholding. Three consecutive z-planes with the highest contrast were mean-projected to yield a single image for quantification. Subsequently, the spot position was selected in each segmented cell based on the co-transfected array marker (tagBFP-LacI) and a disc shaped spot mask with a diameter of 1.6 μm (5 pixels), a ring-shaped background mask and a nuclear mask were used to quantify average intensities in all channels. Spot mask diameters were 1.6 μm (5 pixels) for activators and 3.8 μm (12 pixels) for nascent RNA. Radial profiles were measured by creating masks of concentric rings of pixel-wise increasing radius around the spot position and measuring average intensities up to a radius of 2.9 μm (9 pixels). The minimum value was subtracted from the profiles and they were divided by the local background intensity for normalization. Single cell profiles were averaged for each condition and the minimum value was subtracted. The resulting enrichment score profile gives qualitative information about the accumulated intensity in the spot center. For quantitative comparisons of local concentrations (occupancy and promoter activity plots), average spot intensities were measured in images acquired on the same day with the same imaging parameters. The average intensity in the spot background region was subtracted from the average spot intensity. The resulting intensity in the activator-GFP channel was normalized to the tagBFP-LacI marker channel.

Statistics, data presentation and analysis software

Mean values and 95 % confidence intervals (CI) for time courses of nascent transcripts, BRD4 or fluorescence recovery and for intensity profiles were calculated from single cell data for every time point or radial position from a Student's t-distribution. Pairwise comparisons of the mean for qRT-PCR or relative intensities were done using unpaired, two-sided Student's or Welch's t-tests, respectively. To check for the respective effects of two grouping variables (AD type and presence of optodroplets for half-activation times; occupancy group and sgRNA for the effect of residence time on promoter activation) a two-way ANOVA (type II) was performed. Error bars represent one standard deviation (s. d.) for qRT-PCR experiments and the standard error of the mean (s. e. m.) for half-activation times as indicated. For residence times the mean and CI of k_{off} were determined before calculating the inverse ($1/k_{off}$). Axis breaks were introduced in relative intensity and qRT-PCR plots for conditions with values on very different scales or with outliers and are marked by an interruption of the axis. Box plots show first and third quartile (box), median (bar), data points within 1.5-fold interquartile range (whiskers) and outliers (points). Images were processed with the *NSSQ* package (*56*) available at https://github.com/RippeLab/NSSQ. Exemplary microscopy images were linearly adjusted for visibility using Fiji with the same adjustments applied for all time points (*58*). The *R* software package *NSQFRAP* for the semi-automated FRAP analysis can be downloaded from https://github.com/RippeLab/NSQFRAP.
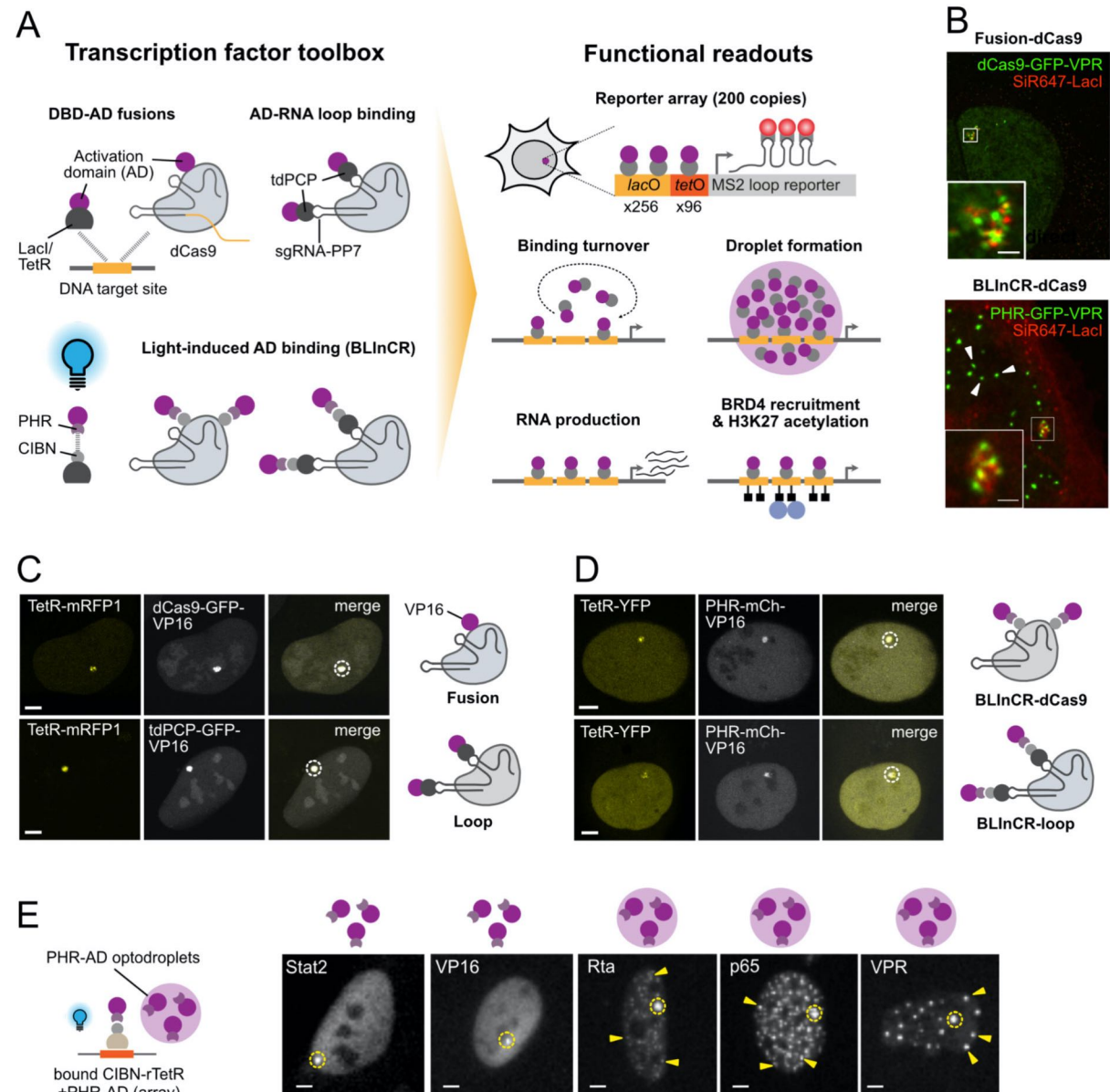
Figures and legends

Fig. 1. A toolbox to dissect transcription activation. (**A**) (r)TetR, LacI and dCas9 as DBDs are combined with different AD as direct fusion constructs ("fusion"), via binding of PP7 coat protein to PP7 RNA loops in the single guide RNA ("loop") or fused to the PHR for light induced interactions with CIBN ("BLInCR"). Activation of these TF architectures was analyzed for the different functional readouts depicted. (**B**) SRRF images of the reporter cluster labeled with SNAPtag-LacI and activated by dCas9-GFP-VPR fusion (top) or BLInCR-dCas9 VPR (bottom). Scale bar, 1.0 μm. (**C**) Confocal microscopy images of transfected U2OS 2-6-3 cells showing targeting of the dCas9 complexes to the reporter array marked with a dashed circle. The *tetO* sites of the reporter array were labeled with co-transfected TetR-mRFP1. (**D**) Microscopy images of successfully enriched PHR-mCherry-VP16 recruited to the *lacO*

repeats using the BLInCR-dCas9 and BLInCR-loop complexes, respectively. TetR-YFP was used as an array marker. Light-dependency of BLInCR-dCas9/BLInCR-loop complex assembly was confirmed in a separate experiment and compared to CIBN-LacI as a previously published reference (**Fig. S1 A, S1 B**). Scale bars, 5 µm. (**E**) Upon illumination PHR-GFP-AD binds to CIBN-rTetR at the promoter and can form ectopic optodroplets depending on the AD. Images of VPR, p65 and Rta show a high propensity to form optodroplets indicated with arrows while they were mostly absent for VP16 and STAT2. The reporter array is marked with a dashed circle. Scale bar: 5 µm.
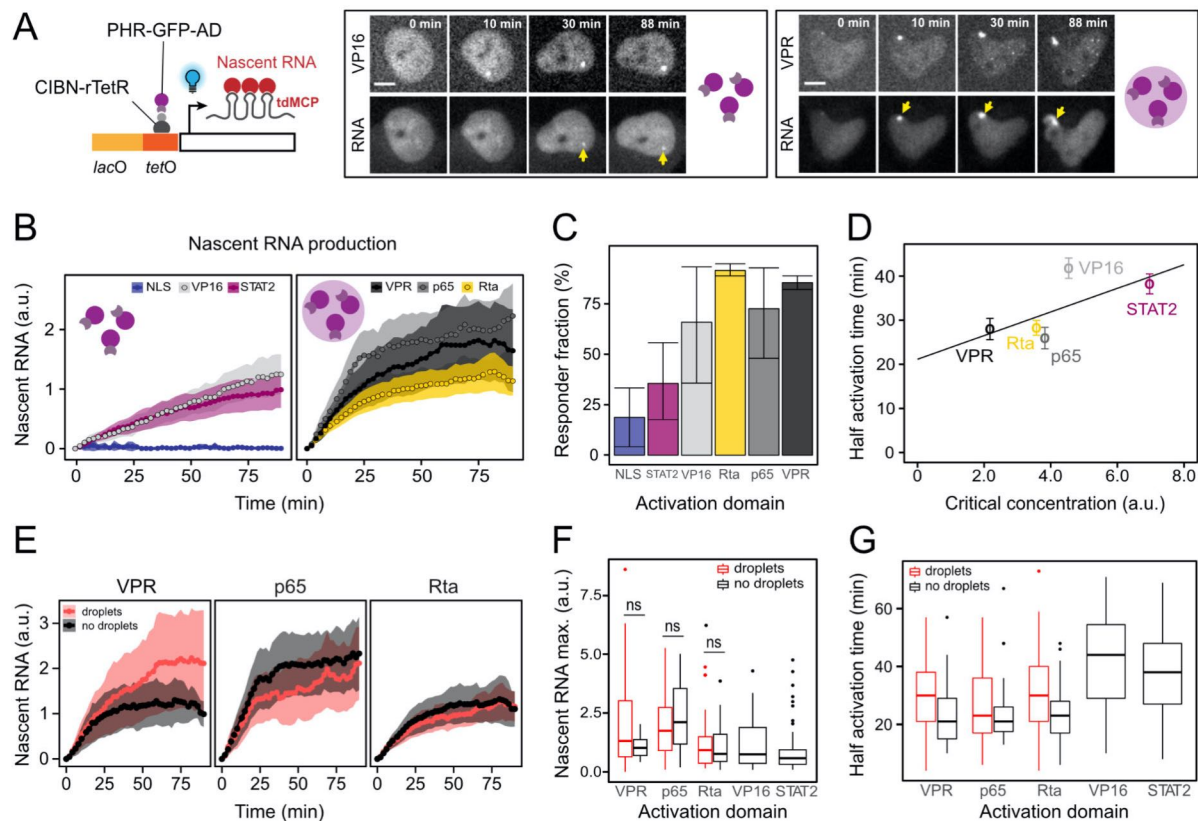
Fig. 2. AD phase separation propensity and activation capacity. Single cell time courses of nascent RNA production were acquired to investigate the relation between droplet formation and transcription activation. (**A**) Light-induced transcription time courses triggered by recruitment of PHR-GFP-AD to CIBN-rTetR (BLInCR-rTetR) at the promoter. Optodroplet formation was monitored in the PHR-GFP-AD channel. Scale bars: 10 µm. (**B**) Average nascent RNA kinetics of responding cells for the different ADs with mean and 95 % CI and n = 31-71 cells per condition. The PHR-GFP-NLS construct served as negative control. (**C**) Fraction of cells with visible enrichment of tdMCP at the promoter spot; bars: min. and max. of 2 or 3 replicate experiments per condition. (**D**) Relationship of phase separation propensity and activation speed. Critical concentrations for optodroplet formation were determined from microscopy images (**Fig. 1E**, **S2 A**). The time to half maximal activation was determined from the single cell trajectories. Error bars represent s. e. m. values. (**E**) Average activation time courses of responding cells visually classified as droplet containing or not with 95 % CI (n = 13-18 cells per condition). (**F**) RNA production measured as the plateau values of the last five time points and excluding non-responding cells for experiments with or without optodroplet formation outside of the reporter array. n. s., not significant, p > 0.05; unpaired two-sided Welch's t-test; n = 13-55 cells per condition. (**G**) Times to half maximal activation of cells classified as droplet containing or not depends on the AD type (p = 3·10⁻⁷). The presence has a neutral or slightly inhibitory effect (p = 0.09, two-way ANOVA) with n = 13-55 cells per condition.
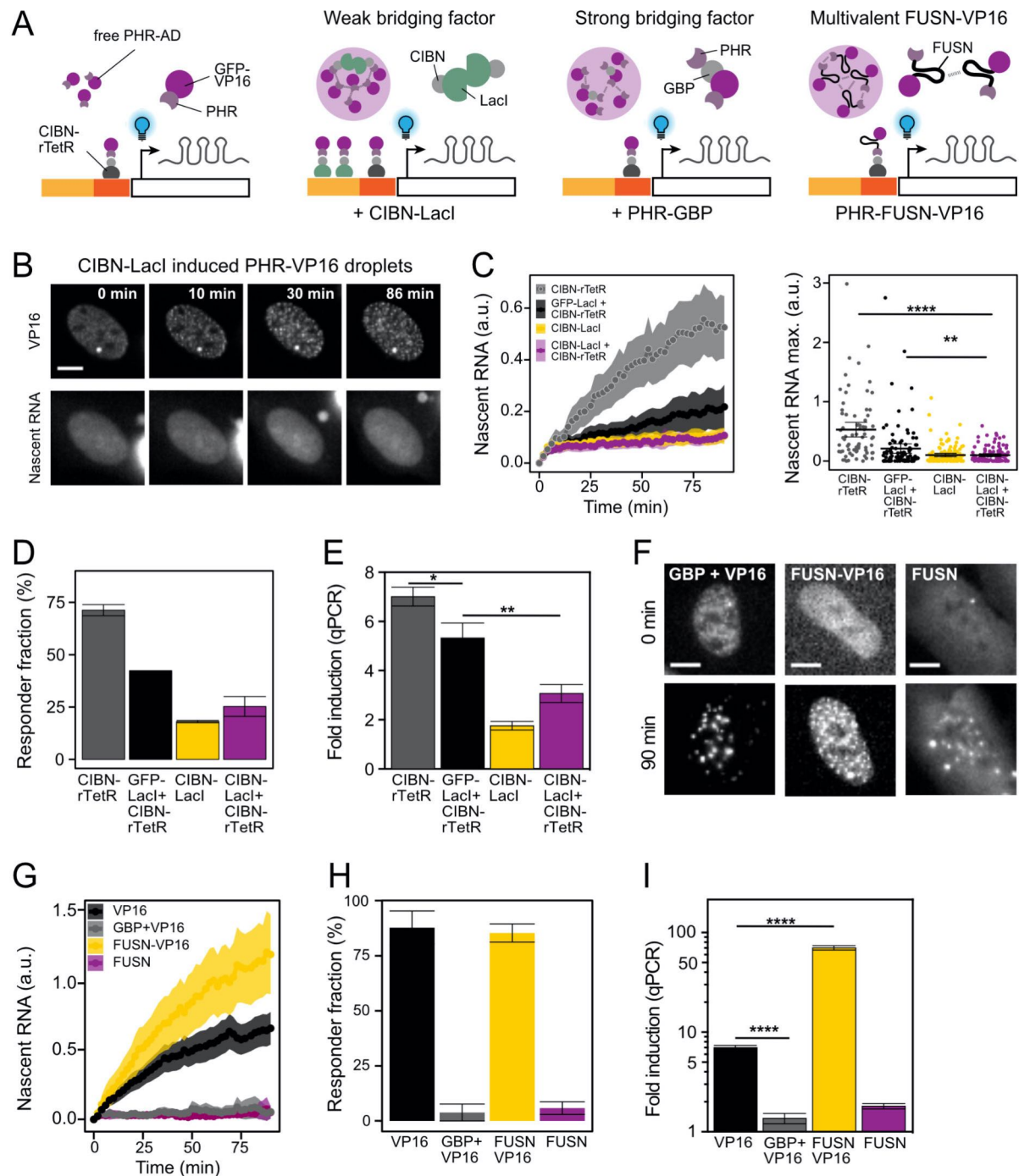
Fig. 3. Induced phase separation of VP16 alters transcriptional response. (**A**) Three independent approaches are depicted that increase the droplet formation propensity of VP16 to study the effect of droplet formation on both single cell nascent RNA and bulk RNA production in the U2OS 2-6-3 reporter cell line. (**B**) Microscopy images of a nascent RNA production time course showing PHR-GFP-VP16 optodroplet induction by CIBN-LacI co-transfection with CIBN-rTetR in a non-responder. (**C**) Left: Averaged nascent RNA time courses and 95 % CI for activation in presence of CIBN-LacI induced optodroplets including responding and non-responding cells (n = 74-126 cells per condition). Right: The maximum values reached at the time course plateau. The activation potential is reduced by CIBN-LacI

with CIBN-rTetR for VP16 as compared to the unperturbed state with only CIBN-rTetR and the GFP-LacI co-transfection control. Dots, single cell RNA time course maxima; bar, mean; error bars, 95 % CI; n. s., not significant, $p > 0.05$; *, $p < 0.05$; **, $p < 0.01$; ****, $p < 0.0001$. The p values were computed with a two-sided Welch's t-test. (**D**) Fraction of cells with visible enrichment of tdMCP at the promoter spot for the CIBN-LacI experiment. Error bars represent minimum and maximum of 2 experiments per condition. (**E**) qRT-PCR of bulk reporter RNA levels 90 min after induction. Data are represented as mean and s. d. of the fold-change induction compared to mock transfected samples and normalized to beta actin mRNA ($n = 3$). *, $p < 0.05$; **, $p < 0.01$ from an unpaired two-sided Student's t-test. (**F**) Image series of cells at the beginning and end of time courses showing optodroplet formation for PHR-GFP-VP16 plus PHR-GBP, PHR-GFP-FUS-VP16 and PHR-GFP-FUS (control). Scale bar: 10 µm. (**G**) Average nascent RNA time courses and 95 % CI for activation by GBP and FUSN induced optodroplets including responding and non-responding cells. PHR-GFP-FUSN was used as control. $n = 24\text{-}154$ cells per condition. (**H**) GBP/FUSN experiments: fraction of cells with visible enrichment of tdMCP at the promoter spot. Error bars represent minimum and maximum of 2 experiments per condition. (**I**) GBP/FUSN experiments: qRT-PCR of bulk reporter RNA levels 90 min after induction. Data is represented as mean and s. d. of fold-change induction compared to mock transfected samples and normalized to beta actin mRNA ($n = 3$). ****, $p < 0.0001$ calculated from an unpaired two-sided Student's t-test.
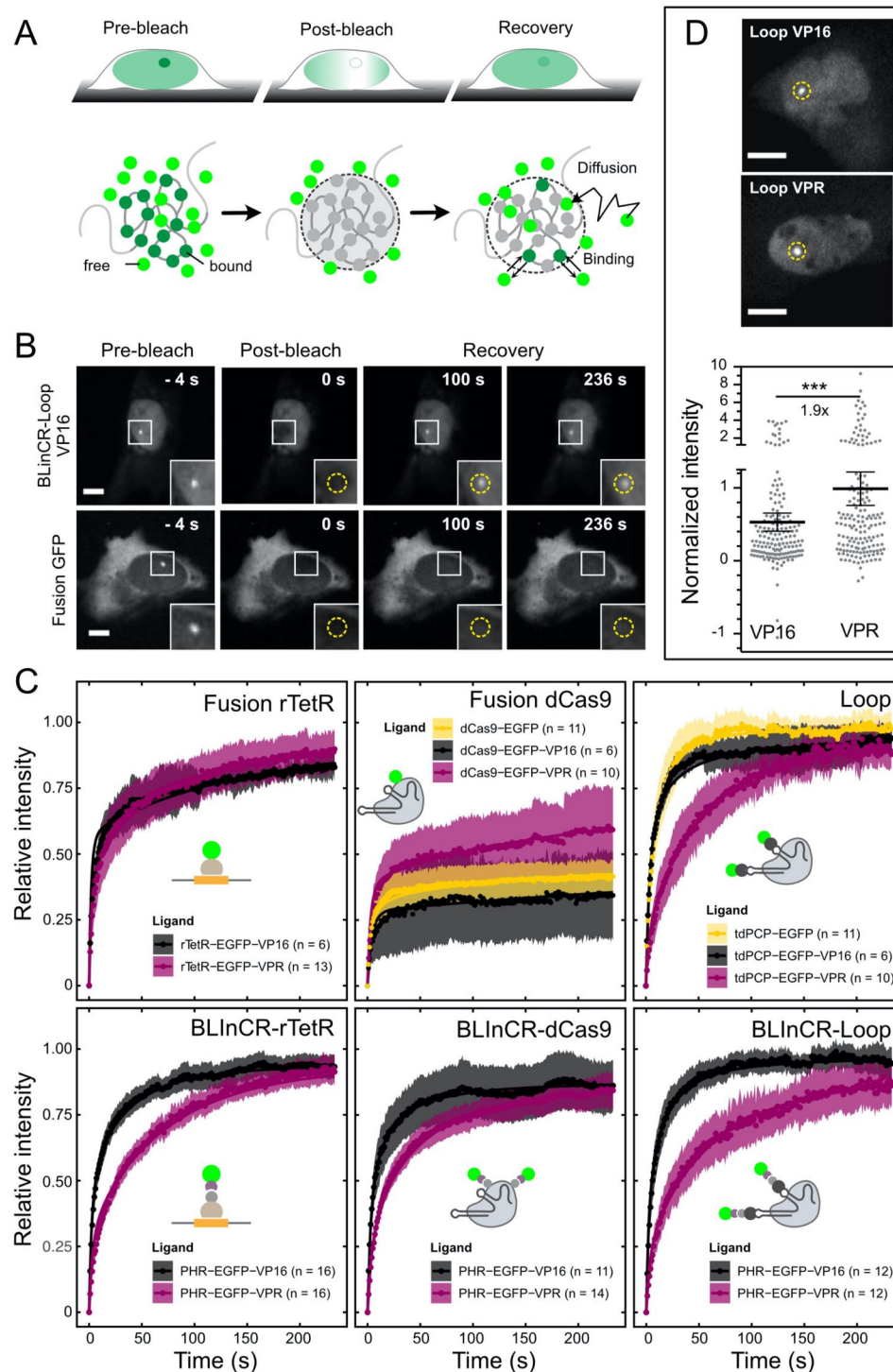
Fig. 4. Dissociation kinetics for TF complexes with different architecture and AD type measured by FRAP. (**A**) Experimental setup for FRAP at clustered binding sites: After bleaching fluorescence recovers by both diffusion of unbleached molecules and exchange of bound molecules at the promoter binding sites in the U2OS 2-6-3 reporter gene array. (**B**) Exemplary FRAP image series for the BLInCR-loop VP16 complex with fast exchange (top) and for dCas9-GFP fusion complex displaying no exchange (bottom) of DNA bound molecules

during the observation period. Scale bar: 10 µm. The dotted circle in the inset marks the reporter array. (**C**) Averaged FRAP curves and 95 % CI. The solid line represents a fit to a reaction-diffusion model for clustered binding sites for GFP-tagged complexes of VP16 and VPR with the indicated DNA binding modules. (**D**) Enrichment of tdPCP-GFP-VP16 and tdPCP-GFP-VPR in the loop complex at the reporter array. GFP signal was background subtracted and normalized to tagBFP-LacI as a marker of the binding site cluster. The 1.9-fold higher signal for VPR indicates and increased amount of indirectly bound molecules. Solid bar, mean; error bars, 95 % CI; n = 164-166 cells per condition; ***, p < 0.001; the p values were calculated from unpaired two-sided Welch's t-test. Scale bar: 10 µm.
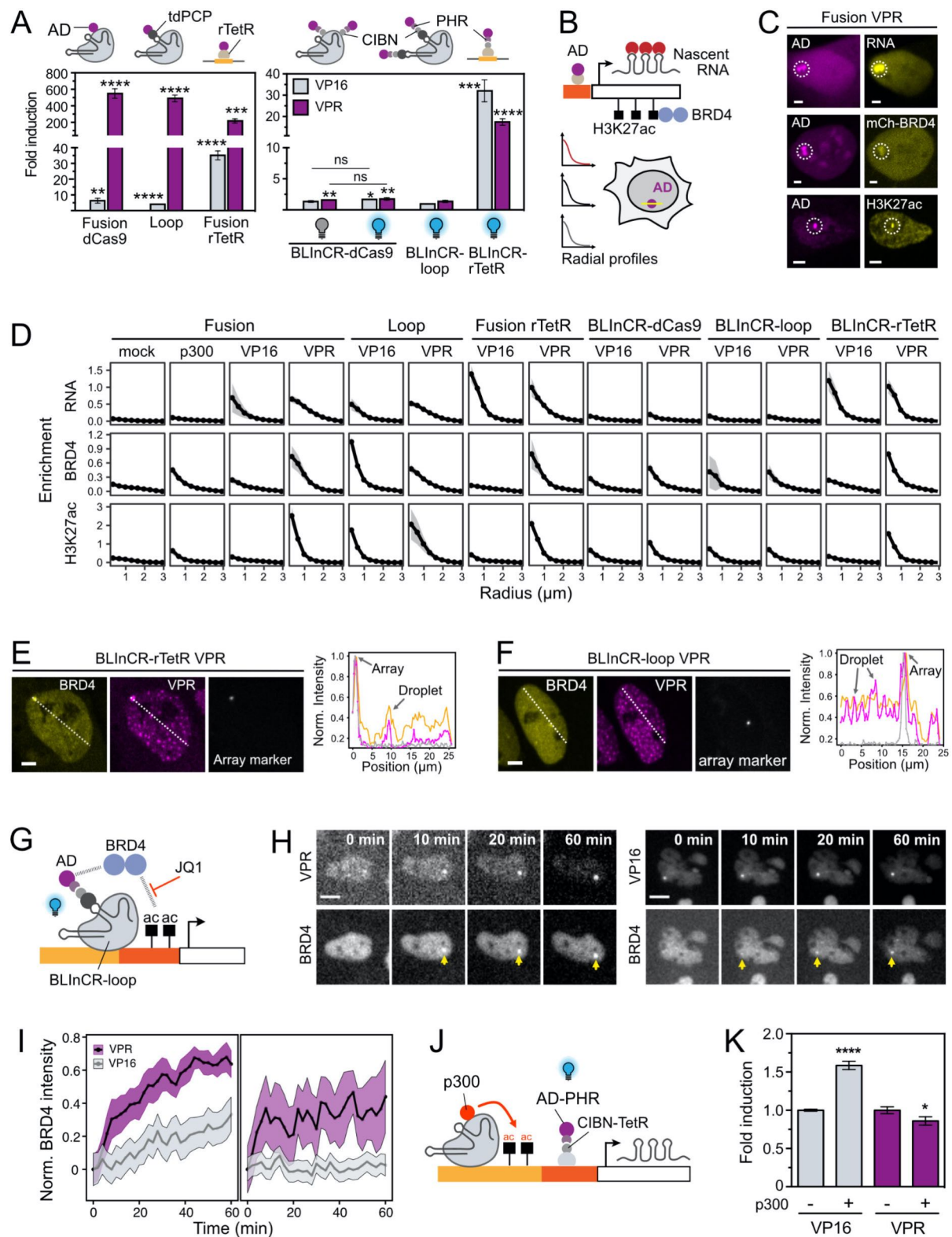
Fig. 5. TF architecture and AD type dependent transcription activation features. (**A**) qRT-PCR of reporter RNA for the different TF constructs at 24 hours after transfection and induction by addition of doxycycline and/or constant blue light illumination. Data are represented as mean and s. d. of fold-change upon induction as compared to mock transfected samples and

normalized to beta actin mRNA (n = 3). Indicated p-values of > 0.05 (n. s.), < 0.05 (*), < 0.01 (**), < 0.001 (***), < 0.0001 (****) are from a two-sided unpaired Student's t-test to the mock condition. (**B**) Enrichment analysis of activation marks and nascent RNA in single cells at 24 h after induction. Activators were recruited to the *tetO* sites and radial enrichment profiles were measured by confocal microscopy of living (nascent RNA, mCherry-BRD4) or fixed (H3K27 acetylation immunostaining) cells. (**C**) Representative microscopy images of cells with *tetO*-targeted dCas9-GFP-VPR complex and the three readouts: nascent RNA visualized with tdMCP-tdTomato, co-transfected mCherry-BRD4 and immunostaining against H3K27ac. The dashed line circle marks the reporter array. Scale bar: 5 µm. (**D**) Computed enrichment profiles for all TFs with either GFP-VP16 or GFP-VPR. Profiles depict the average of n = 16-520 cells per condition. A dCas9-GFP (mock) and dCas9-GFP-p300core fusion were included as additional reference conditions. (**E**) Cells showing partial co-localization of overexpressed mCherry-BRD4 with PHR-GFP-VPR optodroplets upon recruitment to the *tetO* sites via BLInCR-rTetR. Co-transfected tagBFP-LacI marks the reporter. Normalized intensity profiles showing enrichment of mCherry-BRD4 (orange) in some of the VPR optodroplets (pink) and at the array spot marker (grey). Intensities were normalized to the maximum value within each channel profile. Profile positions are indicated by dashed lines. Scale bar: 5 µm. (**F**) Same as panel E but for the BLInCR-loop construct (**G**) Comparison of BRD4 co-recruitment between VP16 and VPR. Light-induced binding of VP16/VPR to the BLInCR-loop complex on both *tetO* and *lacO* sites with/without the bromodomain inhibitor JQ1. The complex does not induce transcription and thus indirect effects on BRD4 binding/acetylation are absent. (**H**) Representative live cell image time series of mCherry-BRD4 enrichment at the reporter (arrows) for VPR (left) or VP16 (right) in the absence of JQ1. Scale bar: 10 µm. (**I**) Time trace of BRD4 signal accumulation at the reporter after light induced VPR/VP16 binding without JQ1 (left) or with JQ1 pre-treatment (right) before induction. Mean values of normalized intensity and 95 % CI are shown with *n* = 10-85 cells per condition. (**J**) Dependency of VP16 and VPR activity on pre-existing histone acetylation. A dCas9-GFP-p300 fusion was constitutively recruited to the *lacO* sites to induce acetylation, followed by light-induced binding of VPR or VP16 to *tetO* via BLInCR-rTetR for 90 minutes to induce transcription. (**K**) qRT-PCR measurements of reporter RNA levels for the experiment outlined in J. Fold induction for the dCas9-GFP-p300 (+) relative to dCas9-GFP (-) control condition is represented as mean and s. d. of 3 replicates. Data were normalized to beta actin mRNA levels and to the RNA level of the dCas9-GFP condition (-). A two-sided unpaired Student's t-test between p300 (+) and control (-) was used to calculate p-values of < 0.05 (*) and < 0.0001 (****).
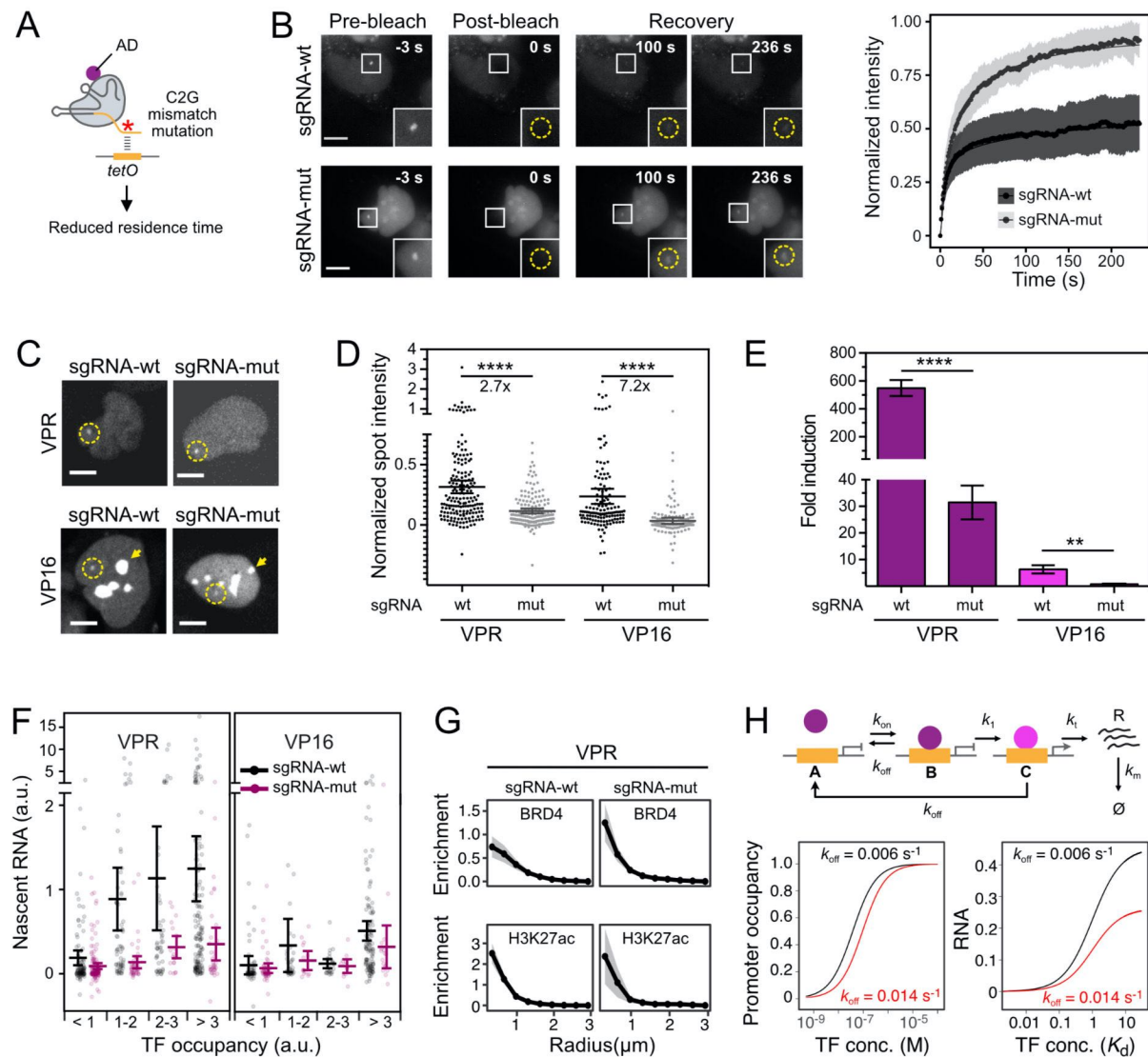
32

Fig. 6. Interdependencies of binding site occupancy, residence time and multivalent interactions during transcription activation. (**A**) dCas9 DNA binding affinity was lowered by introducing a C2G mismatch mutation in the targeting region of the sgRNA. (**B**) FRAP image series (left), averaged recovery curves and 95 % CI (right) of dCas9-GFP-VPR and *tetO* sgRNA-wt (*n* = 10) or sgRNA-mut (*n* = 7). (**C**) Microscopy images showing enrichment of dCas9-GFP-VP16/-VPR at binding sites for sgRNA-wt/mut. Note that the VP16 construct is strongly enriched in nucleoli (arrows). However, this does not affect the analysis of the reporter gene array (dashed circle). (**D**) Enrichment of dCas9-GFP-VP16/VPR with wildtype and mutated sgRNA at the reporter array (*n* = 127-175 cells per condition). Intensities were background subtracted and normalized to tagBFP-LacI marker intensity. Solid bar, mean; error bars, 95 % CI; **** p < 0.0001 from two-sided Welch's t-test. (**E**) qRT-PCR measurements of reporter RNA levels 24 h after transfection for sgRNA-wt/mut. Data show mean and s. d. of fold-change reporter RNA induction compared to mock transfected samples and normalized

33

to beta actin mRNA (n = 3). The data for sgRNA-wt displayed in **Fig. 5 A** are included for comparison. **, p < 0.01; ****, p < 0.0001 from two-sided unpaired Student's t-test. (**F**) Nascent RNA detected via tdMCP-tdTomato normalized to tagBFP-LacI marker intensity. Cells were grouped into groups with equal occupancies determined from the GFP-AD signal normalized to the marker. Transparent dots correspond to values for single cells; mean and 95 % CI are indicated. Note the axis break to visualize the majority of cells as well as the few cells with very high RNA production in the same plot. (**G**) Qualitative detection of activation marks by radial enrichment profiles of mCherry-BRD4 and H3K27ac immunostaining for dCas9-GFP-VPR. Data for sgRNA-wt from **Fig. 5 D** are shown for comparison. Mean and 95 % CI; n = 28-184 cells per condition. (**H**) Model for a multi-step transcription activation mechanism showing the dependence of RNA production at saturated binding on TF residence time (**Supplemental Information**). After TF binding to the promoter (state B) induction of transcription requires another energy consuming transition to state C (indicated by color change) where RNA is produced from the TF-bound promoter with rate k_1. Two different dissociation rates k_{off} = 0.006 s^{-1} (τ_{res} = 167 s) and k_{off} = 0.014 s^{-1} (τ_{res} = 71 s) were compared. Binding site occupancy was computed for k_{on} = 10^5 M^{-1} s^{-1}, corresponding to a K_d of 60 nM and 140 nM, respectively. Steady state RNA levels computed for the two k_{off} values are shown as a function of TF concentration in K_d units, i. e. for the same promoter occupancy.
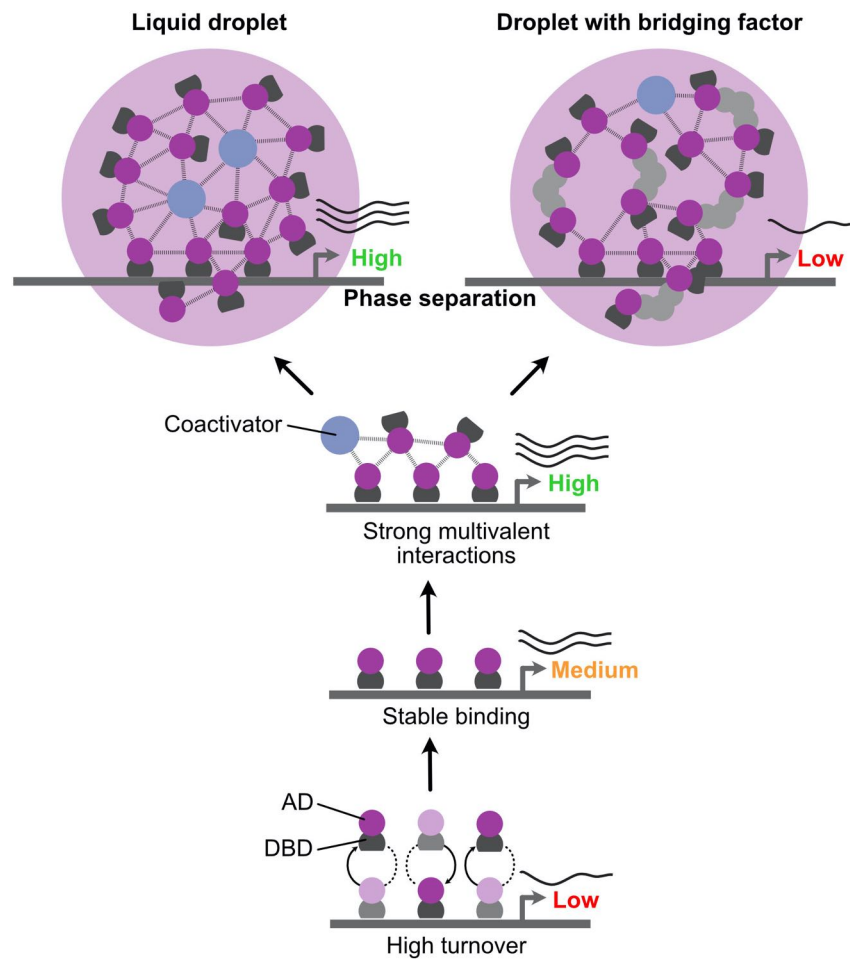
Figure 7. **Integrative model of transcription in dependence of promoter occupancy, residence time and multivalent interactions of the TF.** From bottom to top: Low residence times lead to lower transcription (high turnover vs. stable binding) and multivalent AD interactions increase transcription activation capacity, in part via interactions with coactivators. The formation of phase-separated droplets can further increase the local TF concentration but does not further increase RNA production (top left). Rather, a multimeric TF assembly stabilized by introducing additional interactions via bridging factors can create a repressive subcompartment despite a strong TF enrichment at the promoter (top right).